JCI The Journal of Clinical Investigation

NFκB signaling drives myocardial injury via CCR2^{+} macrophages in a preclinical model of arrhythmogenic cardiomyopathy

Stephen P. Chelko, … , Kory Lavine, Jeffrey E. Saffitz

J Clin Invest. 2024. https://doi.org/10.1172/JCI172014.

Research In-Press Preview **Cardiology** **Immunology**

Nuclear factor kappa-B (NFκB) is activated in arrhythmogenic cardiomyopathy (ACM) patient-derived iPSC-cardiac myocytes under basal conditions and inhibition of NFκB signaling prevents disease in *Dsg2*$^{mut/mut}$ mice, a robust mouse model of ACM. Here, we used genetic approaches and single cell RNA sequencing to define the contributions of immune signaling in cardiac myocytes and macrophages in the natural progression of ACM using *Dsg2*$^{mut/mut}$ mice. We found that NFκB signaling in cardiac myocytes drives myocardial injury, contractile dysfunction, and arrhythmias in *Dsg2*$^{mut/mut}$ mice. NFκB signaling in cardiac myocytes mobilizes macrophages expressing C-C motif chemokine receptor-2 (CCR2^{+} cells) to affected areas within the heart, where they mediate myocardial injury and arrhythmias. Contractile dysfunction in *Dsg2*$^{mut/mut}$ mice is caused both by loss of heart muscle and negative inotropic effects of inflammation in viable muscle. Single nucleus RNA sequencing and cellular indexing of transcriptomes and epitomes (CITE-seq) studies revealed marked pro-inflammatory changes in gene expression and the cellular landscape in hearts of *Dsg2*$^{mut/mut}$ mice involving cardiac myocytes, fibroblasts and CCR2^{+} macrophages. Changes in gene expression in cardiac myocytes and fibroblasts in *Dsg2*$^{mut/mut}$ mice were dependent on CCR2^{+} macrophage recruitment to the heart. These results highlight complex mechanisms of immune injury and regulatory crosstalk between cardiac myocytes, inflammatory cells and fibroblasts in the pathogenesis of ACM.

NFκB signaling drives myocardial injury via CCR2^{+} macrophages in a preclinical model of arrhythmogenic cardiomyopathy

Stephen P. Chelko, PhD,[1,2†α] Vinay R. Penna, BA,[3α] Morgan Engel, BS,[1] Emily A. Shiel, BS,[1] Ann M. Centner, PhD,[1] Waleed Farra, BS,[1] Elisa N. Cannon, BA,[1] Maicon Landim-Vieira, PhD,[1] Niccole Schaible, PhD,[4] Kory Lavine, MD, PhD,[3*] Jeffrey E. Saffitz, MD, PhD[4*]

[*]Co-senior authors
[α]Co-first authors

[1]Department of Biomedical Sciences, Florida State University College of Medicine, Tallahassee, FL
[2]Department of Medicine, Johns Hopkins University School of Medicine, Baltimore, MD
[3]Department of Medicine, Washington University, St. Louis, MO
[4]Departments of Pathology and Emergency Medicine, Beth Israel Deaconess Medical Center and Harvard Medical School,
Boston, MA

Running Title: Innate immune injury in Arrhythmogenic Cardiomyopathy

Conflicts of Interest:

ME, VRP, EAS, WF, AMC, MLV, NS and ENC have no conflicts of interest to disclose; SPC is on the Advisory Board for Rejuvenate Bio and Who We Play For; KL is on the Advisory Board for Medtronic and is a recipient of sponsored research agreements from Amgen, Novartis, Implicit Biosciences, and Kiniksa; and JES is a consultant for Rejuvenate Bio and Implicit Biosciences, and holds a US Patent for the use of buccal cells in the diagnosis of arrhythmogenic cardiomyopathy.

Address correspondence to:

[†]Stephen P. Chelko, PhD
Department of Biomedical Sciences
Florida State University College of Medicine
Tallahassee, FL 32306
Telephone: 850-644-2215
email: stephen.chelko@med.fsu.edu

ABSTRACT

Nuclear factor kappa-B (NFκB) is activated in arrhythmogenic cardiomyopathy (ACM) patient-derived iPSC-cardiac myocytes under basal conditions and inhibition of NFκB signaling prevents disease in *Dsg2*$^{mut/mut}$ mice, a robust mouse model of ACM. Here, we used genetic approaches and single cell RNA sequencing to define the contributions of immune signaling in cardiac myocytes and macrophages in the natural progression of ACM using *Dsg2*$^{mut/mut}$ mice. We found that NFκB signaling in cardiac myocytes drives myocardial injury, contractile dysfunction, and arrhythmias in *Dsg2*$^{mut/mut}$ mice. NFκB signaling in cardiac myocytes mobilizes macrophages expressing C-C motif chemokine receptor-2 (CCR2^{+} cells) to affected areas within the heart, where they mediate myocardial injury and arrhythmias. Contractile dysfunction in *Dsg2*$^{mut/mut}$ mice is caused both by loss of heart muscle and negative inotropic effects of inflammation in viable muscle. Single nucleus RNA sequencing and cellular indexing of transcriptomes and epitomes (CITE-seq) studies revealed marked pro-inflammatory changes in gene expression and the cellular landscape in hearts of *Dsg2*$^{mut/mut}$ mice involving cardiac myocytes, fibroblasts and CCR2^{+} macrophages. Changes in gene expression in cardiac myocytes and fibroblasts in *Dsg2*$^{mut/mut}$ mice were dependent on CCR2^{+} macrophage recruitment to the heart. These results highlight complex mechanisms of immune injury and regulatory crosstalk between cardiac myocytes, inflammatory cells and fibroblasts in the pathogenesis of ACM.

BRIEF SUMMARY

We have uncovered a therapeutically targetable innate immune mechanism regulating myocardial injury and cardiac function in a clinically relevant mouse model of arrhythmogenic cardiomyopathy (ACM).

INTRODUCTION

Arrhythmogenic cardiomyopathy (ACM) is a familial heart muscle disease characterized by the early onset of arrhythmias and increased risk of sudden death followed by progressive myocardial injury ultimately leading to heart failure (1-3). Growing evidence implicates inflammation in the pathogenesis of ACM, but mechanisms of immune-mediated injury are not well understood. Inflammation in ACM has usually been considered in the context of inflammatory cell infiltrates in the heart, which occur frequently and can be extensive (3-5). However, although infiltrating inflammatory cells likely contribute to the pathogenesis of ACM (3, 5), no previous studies have validated this conclusion nor have mechanisms of immune cell-mediated myocardial injury been elucidated.

We have reported that signaling mediated via NFκB, a master regulator of the innate immune response (6), is activated in a mouse model of ACM involving homozygous knock-in of a variant in the gene encoding the desmosomal protein, desmoglein-2 (*Dsg2*$^{mut/mut}$ mice) (6-8). These mice exhibit clinically relevant features seen in ACM patients, including myocardial injury (cardiac myocyte degeneration and replacement by fibrosis), contractile dysfunction, action potential remodeling and ECG changes, ventricular arrhythmias, and inflammation (6-8). Bay 11-7082, a small molecule that inhibits NFκB signaling by blocking degradation of IκBα (9), arrests disease expression and prevents myocardial injury, contractile dysfunction and ECG abnormalities in *Dsg2*$^{mut/mut}$ mice (6). NFκB signaling is also activated under basal conditions *in vitro* in iPSC-cardiac myocytes derived from ACM patients with pathogenic variants in plakophilin-2 (*PKP*2) (6) or *DSG2* (6, 10). These cells produce large amounts of pro-inflammatory mediators under the control of NFκB without provocation and in the absence of inflammatory cells (6, 10).

The fact that ACM patient iPSC-cardiac myocytes mount an innate immune response and inhibition of NFκB prevents development of disease in *Dsg2*$^{mut/mut}$ mice raises a question about the relative pathogenic roles of immune signaling in cardiac myocytes vs. infiltrating inflammatory cells.

Here, we answered this question using a genetic approach. To define the role of immune signaling in cardiac myocytes in ACM, we crossed *Dsg2*$^{mut/mut}$ mice with a mouse line with cardiac myocyte-specific overexpression of a dominant-negative form of IκBα (IκBαΔN) (11), which prevents nuclear translocation of NFκB and, thereby, activation of NFκB-mediated changes in gene expression. The resulting double-mutant mice (*Dsg2*$^{mut/mut}$ X IκBαΔN) express the *Dsg2* pathogenic variant and can activate NFκB signaling in all cell types except cardiac myocytes. Then, to define the pathogenic role of inflammatory cells in ACM, we focused on cells expressing C-C motif chemokine receptor-2 (CCR2), a G-protein coupled receptor for a monocyte chemo-attractant family that includes monocyte chemoattractant protein-1 (MCP-1, aka CCL2). Monocytes and macrophages expressing CCR2 have been implicated in adverse cardiac remodeling and fibrosis (12, 13). Moreover, MCP-1 expression is increased in hearts of *Dsg2*$^{mut/mut}$ mice and in ACM patient iPSC-cardiac myocytes (6). Thus, to define the pathogenic role of CCR2^{+} cells in ACM, we crossed *Dsg2*$^{mut/mut}$ mice with a mouse line with germline deletion of *Ccr2* (*Ccr2*$^{-/-}$ mice) to produce double-mutant *Dsg2*$^{mut/mut}$ X *Ccr2*$^{-/-}$ mice. *Ccr2*$^{-/-}$ mice are fertile and have no apparent phenotype under basal conditions, but monocyte/macrophage mobilization in response to immune-activating agents is impaired and macrophages fail to respond to CCL2 (14).

By comparing phenotypes in *Dsg2*$^{mut/mut}$ mice with double-mutant mouse lines (*Dsg2*$^{mut/mut}$ X IκBαΔN and *Dsg2*$^{mut/mut}$ X *Ccr2*$^{-/-}$) and analyzing single cell RNA sequencing data, we observed that activation of NFκB signaling in cardiac myocytes is a major driver of disease in ACM. Myocardial injury and arrhythmias are mediated, at least in part, by CCR2^{+} macrophages mobilized to areas of myocardial injury and cardiac myocyte death. Additionally, CCR2^{+} macrophages regulate the transcriptional state of cardiac myocytes and fibroblasts in *Dsg2*$^{mut/mut}$ mice. These results highlight the

complex crosstalk between cardiac myocytes, $CCR2^+$ macrophages and fibroblasts in immune injury in ACM.

RESULTS

NFκB signaling in cardiac myocytes mobilizes $CCR2^+$ macrophages to the heart and leads to myocardial injury, contractile dysfunction, and arrhythmias in *Dsg2$^{mut/mut}$* mice. To examine the immune landscape of ACM, we performed flow cytometry on WT and *Dsg2$^{mut/mut}$* hearts at 2, 4, 6, 10, and 16 weeks of age. We observed accumulation of monocytes as early as 4 weeks of age and increased $CCR2^+$ macrophages at 4, 6, 10, and 16 weeks of age in *Dsg2$^{mut/mut}$* hearts. Neutrophils were also increased at early time points. T-cells were reduced at 2 weeks of age, while $CCR2^-$ cardiac resident macrophages were found to be reduced at 4, 6, 10, and 16 weeks of age. B-cells were largely unchanged (**Supplemental Figures 1-2**).

To delineate whether NFκB signaling in cardiac myocytes drives innate immune responses in ACM, we focused on monocytes/macrophages and performed CD68 immunostaining and *Ccr2* RNA *in situ* hybridization on hearts obtained from 16-week-old WT, *Dsg2$^{mut/mut}$* and *Dsg2$^{mut/mut}$* mice crossed with a mouse line expressing a cardiac-specific, dominant-negative form of the inhibitor of kappa B alpha (IκBαΔN).(11) Therefore, these double mutant mice (i.e., *Dsg2$^{mut/mut}$* X IκBαΔN) express an ACM disease allele and a IκBαΔN isoform that is non-phosphorylatable at Ser32/36 and thus, retains inactivated-NFκB within the cytoplasm of cardiac myocytes (15, 16). Areas of myocardial injury and cardiac myocyte death were identified by Evan's blue staining, as previously described (17). We observed accumulation of macrophages expressing *Ccr2* adjacent to areas of myocardial injury in *Dsg2$^{mut/mut}$* hearts. The abundance of these macrophages and extent of myocardial injury was markedly

attenuated in *Dsg2*$^{mut/mut}$ X IκBαΔN hearts, indicating that cardiac myocyte NFκB signaling is a major determinant of monocyte-derived macrophage recruitment, myocardial injury, and cardiac myocyte death (**Figure 1**). Previous work has demonstrated that cardiac myocyte death is an important trigger for monocyte infiltration and CCR2^{+} macrophage activation presumably through release of DAMPs and alarmins (18, 19). Consistent with this concept, we previously demonstrated extracellular localization of high mobility group box-1 (HMGB1) in *Dsg2*$^{mut/mut}$ mice (8). HMGB1 is a non-histone, DNA-binding protein that is associated with necrotic forms of cell death (20) that acts as a damage-associated molecular pattern (DAMP) and initiates local inflammation via activation of macrophages and neutrophils (21).

To define the role of NFκB in cardiac myocytes and CCR2^{+} macrophage recruitment in the pathogenesis of ACM, we compared phenotypes of 8- and 16-week-old WT, *Dsg2*$^{mut/mut}$, *Dsg2*$^{mut/mut}$ X IκBαΔN, and *Dsg2*$^{mut/mut}$ crossed with a mouse line with germline deletion of *Ccr2* (22) (i.e., *Dsg2*$^{mut/mut}$ X *Ccr2*$^{-/-}$ mice). Deletion of *Ccr2* impairs monocyte egress from the bone marrow and spleen, and recruitment of monocytes to peripheral sites (14, 23). As reported previously (6, 7), 8-week-old *Dsg2*$^{mut/mut}$ mice display subclinical cardiac dysfunction (**Supplemental Table 1, Supplemental Figure 3**), while 16-week-old *Dsg2*$^{mut/mut}$ mice show considerable myocardial injury indicated by the presence of extensive fibrosis (which had replaced areas of degenerated cardiac myocytes) (8). We observed marked contractile dysfunction with reduced left ventricular ejection fraction, numerous PVCs and depolarization/repolarization alterations in signal-averaged ECGs (SAECGs) when compared to age-matched WT mice. Conversely, *Dsg2*$^{mut/mut}$ X IκBαΔN mice displayed improved LV systolic function and reduced fibrosis compared to *Dsg2*$^{mut/mut}$ mice. Additionally, *Dsg2*$^{mut/mut}$ X *Ccr2*$^{-/-}$ mice displayed reduced myocardial fibrosis, yet equivalent cardiac function, compared to *Dsg2*$^{mut/mut}$ mice (**Figure 2, Table 1**). No differences in cardiac function and fibrosis were noted in 8-week-old *Dsg2*$^{mut/mut}$ mice

compared to *Dsg2*$^{mut/mut}$ X *Ccr2*$^{-/-}$ and *Dsg2*$^{mut/mut}$ X IκBαΔN mice (**Supplemental Table 1, Supplemental Figure 3**). Both double mutant lines (i.e., *Dsg2*$^{mut/mut}$ X *Ccr2*$^{-/-}$ and *Dsg2*$^{mut/mut}$ X IκBαΔN mice) also displayed a marked reduction in the number of PVCs and less severe alterations in SAECGs compared to *Dsg2*$^{mut/mut}$ mice (**Figure 2**). Consistent with diminished arrhythmogenic substrate(s) in *Dsg2*$^{mut/mut}$ X *Ccr2*$^{-/-}$ and *Dsg2*$^{mut/mut}$ X IκBαΔN mice, infusion of dobutamine (a β_1-adrenergic agonist) and caffeine at 16 weeks of age resulted in fewer induced arrhythmias compared to *Dsg2*$^{mut/mut}$ mice (**Supplemental Figure 4).** These results indicate that activation of NFκB signaling in cardiac myocytes and subsequent CCR2$^+$ macrophage recruitment contribute to progressive myocardial injury, contractile dysfunction, and arrhythmias in *Dsg2*$^{mut/mut}$ mice.

To determine if activation of NFκB signaling in cardiac myocytes also affects myocardial inflammatory cells in ACM, we measured numbers of macrophage subsets in hearts of 16-week-old *Dsg2*$^{mut/mut}$ and *Dsg2*$^{mut/mut}$ X IκBαΔN mice. We focused on macrophages because they are the most abundant immune cell type in mouse and human hearts (24). The number of CD68$^+$ macrophages was greatly increased in hearts from *Dsg2*$^{mut/mut}$ mice compared to WT controls. Furthermore, the percentage of total macrophages expressing LYVE-1 (lymphatic vessel endothelial hyaluronic acid receptor-1), a marker of cardiac resident macrophages (25, 26), was substantially diminished in *Dsg2*$^{mut/mut}$ mice reflecting a shift in macrophage ontogeny favoring recruited CCR2$^+$ monocyte-derived macrophages (**Figure 3**). While the total number of myocardial CD68$^+$ macrophages was equivalent in *Dsg2*$^{mut/mut}$ and *Dsg2*$^{mut/mut}$ X IκBαΔN mice, macrophage populations in *Dsg2*$^{mut/mut}$ X IκBαΔN hearts were more reminiscent of those seen in hearts of WT animals. Specifically, *Dsg2*$^{mut/mut}$ X IκBαΔN mice contained fewer CCR2$^+$ monocyte-derived macrophages and increased numbers of LYVE-1$^+$ macrophages compared to *Dsg2*$^{mut/mut}$ hearts. Taken together, these results indicate that NFκB signaling in cardiac myocytes leads to accumulation of CCR2$^+$ macrophages and loss of cardiac resident macrophages. Such

a shift in cardiac macrophage composition has been associated with enhanced myocardial inflammation and reduced capacity for tissue repair (25). Similar analysis of *Dsg2*$^{mut/mut}$ X *Ccr2*$^{-/-}$ mice revealed a slight reduction in CD68^{+} macrophages compared to *Dsg2*$^{mut/mut}$ mice, and a restoration of LYVE-1^{+} macrophage levels compared to those observed in WT animals (**Figure 3**).

NFκB signaling in cardiac myocytes and CCR2^{+} cells both contribute to the production of inflammatory mediators in *Dsg2*$^{mut/mut}$ mice: Levels of pro-inflammatory cytokines and fibrokines are increased in hearts of 16-week-old *Dsg2*$^{mut/mut}$ mice (6). These mediators are also produced under basal conditions *in vitro* by cardiac myocytes derived from iPSCs from ACM patients harboring variants in *PKP2* or *DSG2* (6, 10). To gain insights into the sources of inflammatory mediators in ACM, we compared cytokine levels in hearts of 8-week-old (**Supplemental Table 2**) and 16-week-old WT, *Dsg2*$^{mut/mut}$ and double mutant mice (**Supplemental Table 3, Figure 4**). Levels of major cytokines of the innate immune response including IL-1β, IL-6 and MCP-1 (aka, CCL2) were increased in hearts of 16-week *Dsg2*$^{mut/mut}$ mice compared to WT mice (complete cytokine expression data for 8- and 16-week-old mice are shown in **Supplemental Tables 2 and 3**). Nearly all of these inflammatory mediators were at least partially normalized in hearts of either *Dsg2*$^{mut/mut}$ X IκBαΔN and *Dsg2*$^{mut/mut}$ X *Ccr2*$^{-/-}$ mice at 16 weeks of age (**Figure 4, Supplemental Table 3**), suggesting that cardiac myocyte NFκB signaling and CCR2^{+} macrophages both trigger expression of inflammatory mediators in *Dsg2*$^{mut/mut}$ mice. One exception was osteopontin (OPN; a pleiotropic and extracellular matrices protein), which was greatly increased in hearts of *Dsg2*$^{mut/mut}$ (6-8 fold) and both double mutant mice (≥4 fold) at 8 and 16 weeks of age. Conversely, 16-week-old *Dsg2*$^{mut/mut}$ X IκBαΔN myocardium showed a stark reduction in OPN levels (1-2 fold), whereas *Dsg2*$^{mut/mut}$ and *Dsg2*$^{mut/mut}$ X *Ccr2*$^{-/-}$ mice maintained these already elevated levels of OPN (≥8 fold, **Supplemental Table 3, Figure 4**). Of note, the fibrosis marker periostin (POSTN) (27, 28) was greatly increased in *Dsg2*$^{mut/mut}$ hearts, but not in *Dsg2*$^{mut/mut}$ X

IκBαΔN or *Dsg2*$^{mut/mut}$ X *Ccr2*$^{-/-}$ hearts at 16 weeks of age, both of which showed considerably reduced amounts of ventricular fibrosis. To gain further insights into the contribution of monocyte recruitment and monocyte-derived CCR2^{+} macrophages in the pathogenesis of ACM, as well as identify cell sources of cytokine production, we utilized single cell transcriptomics.

CITE-seq reveals expansion of CCR2^{+} inflammatory macrophages in hearts of *Dsg2*$^{mut/mut}$ mice: To characterize the transcriptional and cell surface proteomic landscape in ACM, we performed CITE-seq on pooled hearts from 16-week-old WT, *Dsg2*$^{mut/mut}$ and *Dsg2*$^{mut/mut}$ X *Ccr2*$^{-/-}$ mice (**Figure 5A**). After pre-processing and application of quality control filters (**Supplemental Figure 5**) (24, 29), we identified 7 distinct stromal and immune cell types (**Figure 5B, Supplemental Figure 5**) including fibroblasts, endothelial cells, pericytes/smooth muscle cells, monocytes/macrophages, neutrophils and T cells. Differential gene expression analysis revealed cell-type specific transcriptional differences across all major cell types in WT vs. *Dsg2*$^{mut/mut}$ and *Dsg2*$^{mut/mut}$ vs. *Dsg2*$^{mut/mut}$ X *Ccr2*$^{-/-}$ conditions, which were especially prominent in monocytes/macrophages and fibroblasts (**Supplemental Figure 5**). Given robust myocardial inflammation and fibrosis observed in *Dsg2*$^{mut/mut}$ mice and our differential expression analysis, we focused on monocyte/macrophage and fibroblast populations. Within the monocyte/macrophage cluster, we identified several subpopulations including LYVE-1^{+} macrophages, TREM2^{+} macrophages, type-1 and -2 conventional dendritic cells, CCR2^{+} monocytes and macrophages, and LY6C^{low} monocytes (**Figure 5C, Supplemental Figure 6**). Consistent with our immunostaining and *in situ* hybridization studies presented above, cell composition and kernel density analysis revealed increased proportions of CCR2^{+} monocytes and macrophages and decreased LYVE-1^{+} macrophages in *Dsg2*$^{mut/mut}$ hearts compared to WT hearts. These populations were restored to WT levels in *Dsg2*$^{mut/mut}$ X *Ccr2*$^{-/-}$ hearts (**Figure 5D, E**). Differential gene expression analysis between WT vs. *Dsg2*$^{mut/mut}$ monocytes/macrophages revealed profound differences with increased expression of many inflammatory

and fibrosis-associated genes (e.g., *Plac8, Ly6c2, Ccl6, Lgals3*)(25) and decreased expression of resident macrophage-associated genes (e.g., *Cd163, Mrc1, Folr2*) (25, 26) in *Dsg2*$^{mut/mut}$ hearts. These gene expression changes were normalized in *Dsg2*$^{mut/mut}$ X *Ccr2*$^{-/-}$ mice (**Figure 5F, H**). Projection of genes differentially expressed by monocytes/macrophages in *Dsg2*$^{mut/mut}$ hearts within the UMAP space revealed that CCR2^{+} monocytes and macrophages were the primary source of inflammatory mediators enriched in *Dsg2*$^{mut/mut}$ hearts (**Figure 5G**). Pathway enrichment analysis indicated that genes differentially expressed in *Dsg2*$^{mut/mut}$ monocytes/macrophages were associated with increased innate immune activation and fibroblast proliferation, and the enrichment of these pathways was reduced in *Dsg2*$^{mut/mut}$ X *Ccr2*$^{-/-}$ mice (**Figure 5I**).

***Postn*$^{+}$ fibroblasts are expanded in *Dsg2*$^{mut/mut}$ hearts through a CCR2^{+} monocyte- and macrophage-dependent mechanism:** To determine how inhibition of CCR2^{+} monocyte recruitment impacts cardiac fibroblasts in ACM, we further analyzed the fibroblast cluster and identified a number of transcriptionally distinct fibroblast states (**Figure 6A, Supplemental Figure 7**). Cell composition and kernel density analysis revealed a profound increase in *Postn*$^{+}$ fibroblasts and a decrease in *Cxcl14*$^{+}$ fibroblasts in *Dsg2*$^{mut/mut}$ hearts compared to WT hearts (**Figure 6B, Supplemental Figure 7**). We next performed differential gene expression analysis in WT and *Dsg2*$^{mut/mut}$ fibroblasts. We identified increased expression of genes associated with fibrosis pathways and fibrotic injury, such as *Comp*, *Cilp*, and *Fn1* in *Dsg2*$^{mut/mut}$ fibroblasts (30, 31). These genes were partially restored to WT levels in *Dsg2*$^{mut/mut}$ X *Ccr2*$^{-/-}$ mice, suggesting cross-talk between CCR2^{+} monocytes/macrophages and fibroblasts in the progression of myocardial fibrosis in *Dsg2*$^{mut/mut}$ mice (**Figure 6C, E**). Projection of genes differentially expressed in *Dsg2*$^{mut/mut}$ fibroblasts in the UMAP space indicated that *Postn*$^{+}$ fibroblasts are a major fibroblast subset activated in the context of ACM (**Figure 6D**). These data are consistent with a known role of *Postn*$^{+}$ fibroblasts in fibrosis-associated myocardial infarction and

pressure overload (29, 32, 33). Pathway enrichment analysis revealed that genes upregulated in *Dsg2*$^{mut/mut}$ fibroblasts were associated with extracellular matrix remodeling and fibrogenesis and their enrichment was partially reduced in *Dsg2*$^{mut/mut}$ X *Ccr2*$^{-/-}$ hearts (**Figure 6E**). Consistent with our CITE-seq analysis, immunostaining showed POSTN co-localized with CCR2^{+} macrophages and was increased in *Dsg2*$^{mut/mut}$ hearts compared to WT and *Dsg2*$^{mut/mut}$ X *Ccr2*$^{-/-}$ hearts (**Figure 6G-I**).

Single nucleus RNA sequencing reveals a role for CCR2^{+} monocytes and macrophages in cardiac myocyte remodeling in ACM: Cardiac myocytes cannot easily be isolated for single cell sequencing (24). To circumvent this limitation, we performed single nucleus RNA sequencing on pooled hearts from 16-week-old WT, *Dsg2*$^{mut/mut}$ and *Dsg2*$^{mut/mut}$ X *Ccr2*$^{-/-}$ mice (**Figure 7A**). After pre-processing and application of quality control filters (**Supplemental Figure 8A**) (24) we identified 10 distinct cell types (**Figure 7B, Supplemental Figure 8**), including cardiac myocytes, fibroblasts, endothelial cells, pericytes/smooth muscle cells, epicardial cells, macrophages, T-cells and glia-like cells. Differential gene expression analysis revealed cell type-specific transcriptional differences between all major cell types in both WT vs. *Dsg2*$^{mut/mut}$ hearts and *Dsg2*$^{mut/mut}$ vs. *Dsg2*$^{mut/mut}$ X *Ccr2*$^{-/-}$ hearts (**Supplemental Figure 8**). Focused analysis of the cardiac myocytes identified three distinct clusters referred to as CM1 (“healthy” cardiac myocytes), CM2 (“dysfunctional” cardiac myocytes), and CM3 (“conduction system” cardiac myocytes) (24, 34) **(Figure 7C, Supplemental Figure 9**). Cell composition and kernel density analysis showed that the CM2 cluster was increased in *Dsg2*$^{mut/mut}$ hearts compared to either WT or *Dsg2*$^{mut/mut}$ X *Ccr2*$^{-/-}$ hearts (**Figure 7D, E**). Differential gene analysis demonstrated an increase in genes associated with heart failure and inflammation including *Ankrd1*, *Xirp2* and *Tlr4* (24) in *Dsg2*$^{mut/mut}$ cardiac myocytes. Many of these genes were normalized to WT levels in *Dsg2*$^{mut/mut}$ X *Ccr2*$^{-/-}$ cardiac myocytes (**Figure 7F-I**). These findings highlight the complex crosstalk between CCR2^{+} monocytes/macrophages and cardiac myocytes in the pathogenesis of ACM.

Sources of NFκB-activation and mechanisms of contractile dysfunction in ACM:

Examination of 16-week-old *Dsg2*$^{mut/mut}$ X IκBαΔN mice established the importance of canonical NFκB signaling in cardiac myocytes in the pathogenesis of ACM (see **Figure 1**). Importantly, numerous factors may regulate cardiac myocyte NFκB signaling, including cell intrinsic activation stemming from ACM pathogenic variants and crosstalk with innate immune cells, such as CCR2^{+} macrophages. To investigate the relative contribution of each of these sources of NFκB-activation, we immunostained WT control, *Dsg2*$^{mut/mut}$, *Dsg2*$^{mut/mut}$ X *Ccr2*$^{-/-}$, and *Dsg2*$^{mut/mut}$ X IκBαΔN mice with an antibody targeting phosphorylated serine-536 (pSer536) at the C-terminal region of NFκB – a phosphorylation site that is necessary for NFκB nuclear localization and subsequent NFκB-mediated transcription (35). We found elevated NFκB nuclear localization in *Dsg2*$^{mut/mut}$ mice at 8 and 16 weeks of age compared to WT mice (**Supplemental Figure 10**). We further observed reduced myocardial NFκB nuclear-localization in 8- and 16-week-old *Dsg2*$^{mut/mut}$ X *Ccr2*$^{-/-}$ and *Dsg2*$^{mut/mut}$ X IκBαΔN mice (**Supplemental Figure 10**), highlighting possible contributions from both cardiac myocytes and CCR2^{+} macrophages. Interestingly, reduced levels of NFκB nuclear localization were observed in *Dsg2*$^{mut/mut}$ mice at 16 weeks of age compared to 8-week-old *Dsg2*$^{mut/mut}$ mice, suggesting temporal NFκB activation during disease progression.

To evaluate the relative importance of CCR2^{+} macrophage-independent NFκB signaling on contractile dysfunction in ACM, we treated 16-week-old *Dsg2*$^{mut/mut}$ and *Dsg2*$^{mut/mut}$ X *Ccr2*$^{-/-}$ mice with Bay 11-7082, a potent inhibitor of NFκB (6) for 8 weeks and assessed contractile function and arrhythmias before and after treatment. Prior to Bay 11-7082 treatment, *Dsg2*$^{mut/mut}$ and *Dsg2*$^{mut/mut}$ X *Ccr2*$^{-/-}$ mice both showed substantial and roughly equivalent reductions in LV ejection fraction (**Figure 8A**). Vehicle-treated *Dsg2*$^{mut/mut}$ mice showed further deterioration of LV function during the 8-week treatment interval, whereas Bay 11-7082-treated *Dsg2*$^{mut/mut}$ mice showed no further disease progression

and actually exhibited modest improvement in cardiac function and reduced PVC burden (**Figure 8B-E, Supplemental Table 4**). Strikingly, LV ejection fractions in Bay 11-7082 treated *Dsg2*$^{mut/mut}$ X *Ccr2*$^{-/-}$ mice were normalized to levels typically seen in WT mice (**Figure 8B**). Bay 11-7082-treated *Dsg2*$^{mut/mut}$ mice and vehicle-treated *Dsg2*$^{mut/mut}$ X *Ccr2*$^{-/-}$ mice displayed reductions in cardiac fibrosis compared to vehicle treated *Dsg2*$^{mut/mut}$ mice at 24-weeks. Bay 11-7082-treated *Dsg2*$^{mut/mut}$ X *Ccr2*$^{-/-}$ mice showed marked reductions in fibrosis compared to all other treatment groups (**Figure 8F-G**). These observations indicate that LV systolic dysfunction in *Dsg2*$^{mut/mut}$ mice is caused by both CCR2^{+} monocyte and macrophage infiltration as well as an independent source of NFκB signaling. Based on our findings in *Dsg2*$^{mut/mut}$ X IκBαΔN mice (**Figure 1**) and pSer536 NFκB immunostaining (**Supplemental Figure 10**), cardiac myocyte cell intrinsic NFκB signaling represents a likely source. These results have important implications for ACM patients, as anti-inflammatory therapy may be beneficial in patients with established disease.

DISCUSSION

Inflammation has been recognized in ACM for as long as the disease has been known (4, 5). Inflammatory infiltrates are seen at autopsy in the hearts of most ACM patients, and are especially common in ACM patients who died suddenly (3, 5). They typically occur in both ventricles even if macroscopic disease is confined to the RV, and their presence may lead to the misdiagnosis of myocarditis (36, 37). A histological picture reminiscent of acute myocarditis may reflect an active phase of ACM associated with accelerated disease progression (37). Yet, while inflammatory cells likely contribute to the pathogenesis of ACM, no previous studies have validated such a mechanism nor have specific types of inflammatory cells been implicated in myocardial injury and arrhythmias in ACM. Furthermore, iPSC-cardiac myocytes expressing ACM disease variants in *PKP2* (6) or *DSG2*

(10) are known to produce large amounts of pro-inflammatory mediators under the control of NFκB, including primordial cytokines of the innate immune response such as IL-1β, INFγ and TNFα. These cytokines are expressed under basal conditions *in vitro* without stimulation or exogenous provocation and in the absence of inflammatory cells.

These observations raise the question about the relative roles of innate immune responses in cardiac myocytes vs. actions of inflammatory cells in the pathogenesis of ACM. To answer this question, we studied a well-characterized mouse model of ACM (*Dsg2*$^{mut/mut}$ mice) that exhibits progressive myocardial injury (age-dependent loss of heart muscle and replacement by fibrosis), contractile dysfunction and arrhythmias. Using a genetic approach, we defined phenotypes in *Dsg2*$^{mut/mut}$ mice in which either NFκB signaling in cardiac myocytes was prevented or actions of monocytes and macrophages expressing CCR2 were blocked. We discovered complex immune mechanisms in the pathogenesis of ACM involving crosstalk between cardiac myocytes, CCR2^{+} macrophages, and fibroblasts.

The major insight to come from this work is that NFκB signaling in cardiac myocytes is fundamental in the pathogenesis of ACM. Blocking this pathway in cardiac myocytes alone attenuated the ACM disease phenotype in *Dsg2*$^{mut/mut}$ mice. These mice showed little if any myocardial fibrosis, a marked reduction in arrhythmias and ECG depolarization/repolarization abnormalities, preservation of contractile function, and greatly reduced myocardial levels of pro-inflammatory cytokines. These results indicate that NFκB signaling in cardiac myocytes drives myocardial injury, promotes arrhythmias, and stimulates production of pro-inflammatory mediators.

NFκB signaling in cardiac myocytes also had a profound impact on populations of myocardial inflammatory cells and fibroblasts in *Dsg2*$^{mut/mut}$ mice. The hearts of these mice contained reduced numbers of LYVE-1^{+} cardiac resident macrophages, and greatly increased numbers of pro-inflammatory

CCR2^{+} macrophages and pro-fibrotic *Postn*$^{+}$ fibroblasts compared to WT mice. This highly pro-inflammatory cellular landscape was greatly attenuated when NFκB signaling in cardiac myocytes was blocked in *Dsg2*$^{mut/mut}$ X IκBαΔN mice. These findings strongly suggest that signals emanating from cardiac myocytes in *Dsg2*$^{mut/mut}$ mice cause CCR2^{+} macrophages to accumulate in the heart and promote development of a subset of fibroblasts known to participate in myocardial fibrosis.

To gain insights into the actions of CCR2^{+} cells, we analyzed phenotypes in *Dsg2*$^{mut/mut}$ mice with germline deletion of *Ccr2*. As seen in *Dsg2*$^{mut/mut}$ X IκBαΔN mice in which NFκB signaling in cardiac myocytes was blocked, *Dsg2*$^{mut/mut}$ X *Ccr2*$^{-/-}$ mice exhibited little if any myocardial fibrosis. They also contained fewer *Postn*$^{+}$ cells in their hearts than *Dsg2*$^{mut/mut}$ mice and showed pronounced reductions in arrhythmias and cytokine levels. These observations indicate that CCR2^{+} cells mediate myocardial injury and promote arrhythmias, as these disease features were clearly mitigated in *Dsg2*$^{mut/mut}$ X *Ccr2*$^{-/-}$ mice. They also suggest that the greatly reduced myocardial injury seen in *Dsg2*$^{mut/mut}$ X IκBαΔN mice was due mainly, if not entirely, to diminished numbers of CCR2^{+} macrophages in these hearts. Thus, NFκB signaling in cardiac myocytes from ACM subjects stimulates CCR2^{+} cells to accumulate in the heart where they mediate myocardial injury and promote arrhythmias.

Despite the distinct lack of myocardial fibrosis in *Dsg2*$^{mut/mut}$ X *Ccr2*$^{-/-}$ mice, LV contractile function was reduced to an extent seen in *Dsg2*$^{mut/mut}$ mice at 16 weeks of age. This observation suggested that NFκB signaling in cardiac myocytes, which was presumably unaffected in *Dsg2*$^{mut/mut}$ X *Ccr2*$^{-/-}$ mice, caused contractile dysfunction related to negative inotropic effects of inflammation in viable myocardium. Such a mechanism was supported by studies showing that treating 16-week-old *Dsg2*$^{mut/mut}$ X *Ccr2*$^{-/-}$ mice with the NFκB blocker Bay 11-7082 fully normalized contractile function. These observations suggest that contractile dysfunction in ACM patients is related not only to loss of myocardium and its replacement by fibrofatty scar tissue, but to potentially reversible changes in viable

myocardium caused by persistent innate immune signaling. If so, then anti-inflammatory therapy in ACM patients with established disease might result in, at least, some recovery of contractile function.

Results of CITE-seq and snRNA-seq studies revealed additional insights highlighting remarkable crosstalk between cardiac myocytes, $CCR2^{+}$ macrophages and $Postn^{+}$ fibroblasts. For example, *Tlr4*, the gene for the major pattern recognition receptor on cardiac myocytes, was one of the most highly upregulated genes in cardiac myocytes in $Dsg2^{mut/mut}$ mice, consistent with the chronic, non-resolving NFκB signaling known to occur in cardiac myocytes in ACM. Yet, *Tlr4* expression was not increased in cardiac myocytes in $Dsg2^{mut/mut}$ X $Ccr2^{-/-}$ mice. Similarly, *Postn* expression was greatly increased in fibroblasts in $Dsg2^{mut/mut}$ mice but not in $Dsg2^{mut/mut}$ X $Ccr2^{-/-}$ mice. These results suggest that signals from $CCR2^{+}$ cells directly or indirectly regulate gene expression in cardiac myocytes and fibroblasts in $Dsg2^{mut/mut}$ mice.

The results of this study reveal insights into mechanisms of immune injury in ACM and demonstrate bidirectional interactions between cardiac myocytes, inflammatory cells, and fibroblasts. They also identify potential drug targets and strategies. However, as provocative as these findings may be, major questions remain unanswered and may serve as priorities for future research. For example, how variants in desmosomal genes lead to persistent activation of innate immune responses that fail to resolve is yet not known. Glycogen synthase kinase 3β (GSK3β), which is aberrantly activated in cardiac myocytes in ACM due to altered Wnt/β-catenin pathways (7, 38, 39), could be a mechanistic link. Activation of GSK3β has been shown to promote inflammation through NFκB, whereas inhibition of GSK3β limits inflammation (40-42). Another unanswered question concerns the pathogenic roles of specific inflammatory mediators produced by cardiac myocyte and/or inflammatory cells in ACM. Progress in this area could impact future drug discoveries. Related unanswered questions concern the specific signals used by cardiac myocytes to mobilize inflammatory cells and orchestrate their injurious

activities in ACM, and mechanisms used by $CCR2^+$ cells that regulate gene expression in cardiac myocytes and fibroblasts. Finally, it should be emphasized that these studies focused only on the role of $CCR2^+$ cells in *Dsg2*$^{mut/mut}$ mice. Other types of inflammatory cells undoubtedly participate in the pathogenesis of ACM as well.

Studies here were performed entirely in genetically manipulated mouse models of ACM. Previous studies of ACM patient-derived iPSC-cardiac myocytes suggest that inflammatory signaling mediated by NFκB is activated in a cell-autonomous fashion in ACM (6, 10). To determine if NFκB is activated in cardiac myocytes in patients with ACM, we performed parallel studies in post-mortem hearts from ACM patients who died suddenly. As reported in Bueno-Beti et al,(43) we observed nuclear signal for RelA/p65 in cardiac myocytes in a great majority of hearts from patients with ACM, indicating active NFκB signaling in cardiac myocytes at time of death. This was associated with a palpable increase in the number of $CCR2^+$ cells in ACM patient hearts compared to hearts of age-matched controls with no history of heart disease. We also found evidence of activation of NFκB signaling in buccal mucosa cells obtained from young ACM patients at the time they first exhibited clinical manifestations of disease (43). Taken together, our insights gained here through studies of experimental models (combined with patient data reported by Bueno-Beti and colleagues) provide a compelling rationale for the potential benefit of anti-inflammatory therapy in ACM.

METHODS

Sex as a biological variable: this study utilized both male and female mice. Our study examined male and female mice, and similar findings are reported for both sexes.

Generation of double-mutant ACM mouse models: To create ACM mice in which activation of NFκB signaling in cardiac myocytes was prevented, we crossed *Dsg2*$^{mut/mut}$ mice with mice with transgenic cardiac myocyte-specific overexpression of a dominant-negative form of the NFκB pathway protein IκBα involving deletion of 36 NH_2-terminal amino acids (generously supplied by Dr. Douglas Mann) (11). This N-terminal deletion (ΔN) prevents phosphorylation of Ser32/36 in IκBα and subsequent nuclear localization of NFκB in cardiac myocytes (15, 16). This line has been used to define the role of NFκB in cardiac myocyte apoptosis following ischemia (11). Mice were crossbred to obtain a line with *Dsg2*-mutant homozygosity and cardiac myocyte-specific overexpression of dominant-negative IκBα (IκBαΔN) (11), thus creating *Dsg2*$^{mut/mut}$ X IκBαΔN double-mutant mice. To produce ACM mice, in which actions of $CCR2^+$ cells were blocked, we crossed *Dsg2*$^{mut/mut}$ mice with mice with germline deletion of murine *Ccr2 (Ccr2*$^{-/-}$, Jackson Laboratory, strain: 017586) (22). These mice were crossbred to double homozygosity to produce *Dsg2*$^{mut/mut}$ X *Ccr2*$^{-/-}$ double-mutant mice.

Characterization of disease phenotypes: Initial immune phenotyping by flow cytometry was performed in 2-week, 4-week, 6-week, 10-week, and 16-week-old WT and *Dsg2*$^{mut/mut}$ mice. Additionally, phenotypes in *Dsg2*$^{mut/mut}$ and the two double-mutant lines were studied at 8 and 16 weeks of age and compared to age-matched wild-type (WT) controls. As previously reported, 8-week-old *Dsg2*$^{mut/mut}$ mice exhibit only a modest disease phenotype consisting of a few premature ventricular complexes (PVCs), minimally reduced contractile function and little if any myocardial injury (6, 7). By 16 weeks of age, however, they show marked arrhythmias, marked contractile dysfunction and extensive myocardial replacement fibrosis (7). Accordingly, to define the effects of NFκB signaling in cardiac myocytes and actions of $CCR2^+$ cells in the development of the ACM phenotype, all mice underwent echocardiographic and ECG analyses at 8 and 16 weeks of age. Then, hearts obtained from 16-week-old animals were further analyzed by: 1) histology to measure the amount of ventricular fibrosis; 2)

immunohistochemistry and RNA-scope *in situ* hybridization to measure the number of specific subsets of macrophages; 3) Evan's Blue staining and immunohistochemistry to assess cardiac myocyte death; 4) cytokine arrays to measure the levels of various inflammatory mediators; 5) single nuclei RNA sequencing (snRNA-seq) and cellular indexing of transcriptomes and epitomes (CITE-seq) to characterize gene expression and related changes in specific cells types in the heart including macrophages, fibroblasts and cardiac myocytes; and 6) infusion of caffeine and dobutamine for arrhythmia induction studies. Detailed descriptions of these methods are included in supplemental materials.

In vivo drug treatment: The effects of Bay 11-7082, a small molecule inhibitor of NFκB, on left ventricular contractile function were compared in *Dsg2*$^{mut/mut}$ mice and *Dsg2*$^{mut/mut}$ X *Ccr2*$^{-/-}$ mice to determine the extent to which inhibition of NFκB signaling could prevent further disease progression and promote recovery of cardiac function. 16-week-old *Dsg2*$^{mut/mut}$ and *Dsg2*$^{mut/mut}$ X *Ccr2*$^{-/-}$mice underwent echocardiography before being implanted with subcutaneous osmotic minipumps (Alzet, Model 1004), as previously described (6). They received either vehicle or drug (50 µg/µL Bay11-7082 dissolved in 65% dimethyl sulfoxide, 15% ethanol, and 20% 1X PBS). Drug-treated mice received 5 mg/kg/day Bay11-7082 via continuous infusion (0.11 µL/hr for 28 days); vehicle-treated mice received an equivalent volume of vehicle for 28 days. Minipumps were replaced at 20 weeks of age, and treatment was continued for an additional 4 weeks (**Supplemental Figure 11**). Final echocardiograms were obtained in both groups at 24 weeks of age.

Statistical analysis: All data are presented as mean±SEM; n-values and the statistical analyses performed for each experiment are indicated in figure legends and tables. Gaussian distributions were assumed considering sample sizes (n≥10). Differences in measured variables were assessed with Mann-Whitney or 1-way ANOVA with Tukey post-hoc analysis. A P-value of <0.05 was considered

statistically significant. All statistical analyses were analyzed using GraphPad Prism (v9.2) software. Raw sequence files and processed .rds object that support the findings of this study are available on the Gene Expression Omnibus (GSE228048). Code to reproduce the figures derived from the sequencing data will be available on the Lavine Lab Github or upon request to the authors.

Study approval: All experiments in this study conformed to the National Institutes of Health Guide for the Care and Use of Laboratory Animals (NIH publication no. 85-23, revised 1996). All protocols were approved by the Animal Care and Use Committees at Florida State University and Washington University in St. Louis. All animals were housed in a 12-hour-light/dark cycle, climate-controlled facility with *ad libitum* access to water and standard rodent chow.

Data availability: All raw data are provided in the supplement. Additionally, raw sequence files and processed .rds object that support the findings of this study are available on the Gene Expression Omnibus (GSE228048). Code to reproduce the figures derived from the sequencing data will be available on the Lavine Lab Github or upon request to the authors.

ACKNOWLEDGMENTS

We thank Dr. Douglas Mann (Washington University School of Medicine in St. Louis) from whom we acquired the IκBαΔN mice. This work was supported by an American Heart Association Career Development Award (19CDA34760185, S.P. Chelko); a National Institutes of Health grant (R01-HL148348, J.E. Saffitz); a Washington University in St. Louis Rheumatic Diseases Research Resource-Based Center grant (NIH P30AR073752, K. Lavine); a National Institutes of Health grant (R35 HL161185, K. Lavine); a Leducq Foundation Network grant (#20CVD02, K. Lavine); a Burroughs Welcome Fund grant (1014782, K. Lavine); a Children's Discovery Institute of Washington University

and St. Louis Children's Hospital grant (CH-II-2015-462, CH-II-2017-628, PM-LI-2019-829, K. Lavine); a Foundation of Barnes-Jewish Hospital grant (8038-88, K. Lavine); and generous gifts from Washington University School of Medicine (K. Lavine). V. Penna is supported by a National Institutes of Health grant (5T32AI007163-44, V. Penna).

REFERENCES

1. Corrado D. Arrhythmogenic right ventricular cardiomyopathy: evaluation of the current diagnostic criteria and differential diagnosis. *Eur Heart J.* 2020;41(14):1414–29.
2. Marcus FI. Diagnosis of arrhythmogenic right ventricular cardiomyopathy/dysplasia: proposed modification of the Task Force Criteria. *Eur Heart J.* 2010;31(7):806-14.
3. Corrado D. Spectrum of clinicopathologic manifestations of arrhythmogenic right ventricular cardiomyopathy/dysplasia: a multicenter study. *J Am Coll Cardiol.* 1997;30(6):1512-20.
4. Marcus FI. Right ventricular dysplasia: a report of 24 adult cases. *Circulation.* 1982;65(2):384-98.
5. Fontaine G. The arrhythmogenic right ventricle. Dysplasia versus cardiomyopathy. *Heart Vessels.* 1995;10(5):227-35.
6. Chelko SP. Therapeutic Modulation of the Immune Response in Arrhythmogenic Cardiomyopathy. *Circulation.* 2019;140(18):1491-505.
7. Chelko SP. Central role for GSK3β in the pathogenesis of arrhythmogenic cardiomyopathy. *JCI Insight.* 2016;1(5):e85923.
8. Chelko SP. Exercise triggers CAPN1-mediated AIF truncation, inducing myocyte cell death in arrhythmogenic cardiomyopathy. *Sci Transl Med.* 2021;13(581):eabf0891.
9. Coghlan MP. Selective small molecule inhibitors of glycogen synthase kinase-3 modulate glycogen metabolism and gene transcription. *Chem Biol.* 2000;7(10):793-803.
10. Hawthorne RN. Altered Electrical, Biomolecular, and Immunologic Phenotypes in a Novel Patient-Derived Stem Cell Model of Desmoglein-2 Mutant ARVC. *J Clin Med.* 2021;10(14):3061.
11. Misra A. Nuclear factor-kappaB protects the adult cardiac myocyte against ischemia-induced apoptosis in a murine model of acute myocardial infarction. *Circulation.* 2003;108(25):3075-8.
12. Braga TT. CCR2 contributes to the recruitment of monocytes and leads to kidney inflammation and fibrosis development. *Inflammopharmacology.* 2018;26(2):403-11.
13. F Heymann CT, F Tackle. Monocytes and macrophages as cellular targets in liver fibrosis. *Inflamm Allergy Drug Targets.* 2009;8(4):307-18.
14. Boring L. Impaired monocyte migration and reduced type-1 (Th1) cytokine responses in C-C chemokine receptor 2 knockout mice. *J Clin Invest.* 1997;100(10):2552-61.
15. Wang X. Post-translational Modifications of IκBα: The State of the Art. *Front Cell Dev Biol.* 2020;8:574706.
16. Traenckner EB. Phosphorylation of human I kappa B-alpha on serines 32 and 36 controls I kappa B-alpha proteolysis and NF-kappa B activation in response to diverse stimuli. *EMBO J.* 1995;14(12):2876-83.
17. Gardner BB, Swaggart KA, Kim G, Watson S, and McNally EM. Cardiac function in muscular dystrophy associates with abdominal muscle pathology. *J Neuromuscul Dis.* 2015;2(1):39-49.
18. Li W, Feng G, Gauthier JM, Lokshina I, Higashikubo R, Evans S, et al. Ferroptotic cell death and TLR4/Trif signaling initiate neutrophil recruitment after heart transplantation. *J Clin Invest.* 2019;129(6):2293-304.
19. Li W, Hsiao HM, Higashikubo R, Saunders BT, Bharat A, Goldstein DR, et al. Heart-resident CCR2. *JCI Insight.* 2016;1(12).
20. Klune JR, Dhupar R, Cardinal J, Billiar TR, and Tsung A. HMGB1: endogenous danger signaling. *Mol Med.* 2008;14(7-8):476-84.
21. Chen R, Kang R, and Tang D. The mechanism of HMGB1 secretion and release. *Exp Mol Med.* 2022;54(2):91-102.
22. Saederup N. Selective chemokine receptor usage by central nervous system myeloid cells in CCR2-red fluorescent protein knock-in mice. *PLoS One.* 2010;5(10):e13693.

23. Petermann M. CCR2 Deficiency Impairs Ly6Clo and Ly6Chi Monocyte Responses in Orientia tsutsugamushi Infection. *Front Immunol.* 2021;12:670219.
24. Koenig AL. Single-cell transcriptomics reveals cell-type-specific diversification in human heart failure. *Nat Cardiovasc Res.* 2022;1(3):263-80.
25. Bajpai G. Tissue Resident CCR2- and CCR2+ Cardiac Macrophages Differentially Orchestrate Monocyte Recruitment and Fate Specification Following Myocardial Injury. *Circ Res.* 2019;124(2):263-78.
26. Leid J. Primitive Embryonic Macrophages are Required for Coronary Development and Maturation. *Circ Res.* 2016;118(10):1498-511.
27. Zhao S. Periostin expression is upregulated and associated with myocardial fibrosis in human failing hearts. *J Cardiol.* 2014;63(5):373-8.
28. Gil H. Defining the timeline of periostin upregulation in cardiac fibrosis following acute myocardial infarction in mice. *Sci Rep.* 2022;12(1):21863.
29. Lavine K. Targeting Immune-Fibroblast Crosstalk in Myocardial Infarction and Cardiac Fibrosis [preprint]. https://doi.org/10.21203/rs.3.rs-2402606/v1;Posted on Res Sq January 26, 2023.
30. Nanri Y. Cross-Talk between Transforming Growth Factor-β and Periostin Can Be Targeted for Pulmonary Fibrosis. *Am J Respir Cell Mol Biol.* 2020;62(2):204-16.
31. Park S. Cardiac Fibrosis Is Associated With Decreased Circulating Levels of Full-Length CILP in Heart Failure. *JACC Basic Transl Sci.* 2020;5(5):432-43.
32. Alexanian M. A transcriptional switch governs fibroblast activation in heart disease. *Nature.* 2021;595(7867):438-43.
33. Kanisicak O. Genetic lineage tracing defines myofibroblast origin and function in the injured heart. *Nat Commun.* 2016;7:12260.
34. Chaffin M. Single-nucleus profiling of human dilated and hypertrophic cardiomyopathy. *Nature.* 2022;608(7921):174-80.
35. Kwon HJ, Choi GE, Ryu S, Kwon SJ, Kim SC, Booth C, et al. Stepwise phosphorylation of p65 promotes NF-κB activation and NK cell responses during target cell recognition. *Nat Commun.* 2016;7:11686.
36. Scheel PJ. Arrhythmogenic Right Ventricular Cardiomyopathy Presenting as Clinical Myocarditis in Women. *Am J Cardiol.* 2021;145:128-34.
37. Lopez-Ayala JM. Genetics of myocarditis in arrhythmogenic right ventricular dysplasia. *Heart Rhythm.* 2015;12(4):766-73.
38. Garcia-Gras E. Suppression of canonical Wnt/beta-catenin signaling by nuclear plakoglobin recapitulates phenotype of arrhythmogenic right ventricular cardiomyopathy. *J Clin Invest.* 2006;116(7):2012-21.
39. Asimaki A. Identification of a new modulator of the intercalated disc in a zebrafish model of arrhythmogenic cardiomyopathy. *Sci Transl Med.* 2014;6(240):240ra74.
40. Besse S. Early Protective Role of Inflammation in Cardiac Remodeling and Heart Failure: Focus on TNFα and Resident Macrophages. *Cells.* 2022;11(7):1249.
41. Richard S Jope CJY, Eléonore Beurel. Glycogen Synthase Kinase-3 (GSK3): Inflammation, Diseases, and Therapeutics. *Neurochem Res.* 2007;32(4-5):577-95.
42. Asatryan B. Inflammation and Immune Response in Arrhythmogenic Cardiomyopathy: State-of-the-Art Review. *Circulation.* 2021;144(20):1646-55.
43. Bueno-Beti C, Tafuni A, Chelko SP, Sheppard MN, Field E, Tollit J, et al. Innate immune signaling in hearts and buccal mucosa cells of patients with arrhythmogenic cardiomyopathy. *Heart Rhythm O2.* 2023;4(10):650-9.
44. Faisal Syed AD, Harvey S Hahn. Murine echocardiography: a practical approach for phenotyping genetically manipulated and surgically modeled mice. *J Am Soc Echocardiogr.* 2005;18(9):982-90.
45. Monnerat G, Alarcón ML, Vasconcellos LR, Hochman-Mendez C, Brasil G, Bassani RA, et al. Author Correction: Macrophage-dependent IL-1β production induces cardiac arrhythmias in diabetic mice. *Nat Commun.* 2021;12(1):7261.
46. Kadyrov FF. Hypoxia Sensing in Resident Cardiac Macrophages Regulates Monocyte-Derived Macrophage Fate Specification following Myocardial Infarction [preprint]. https://doi.org/10.1101/2022.08.04.502542; Posted on bioRxiv August 5, 2022.

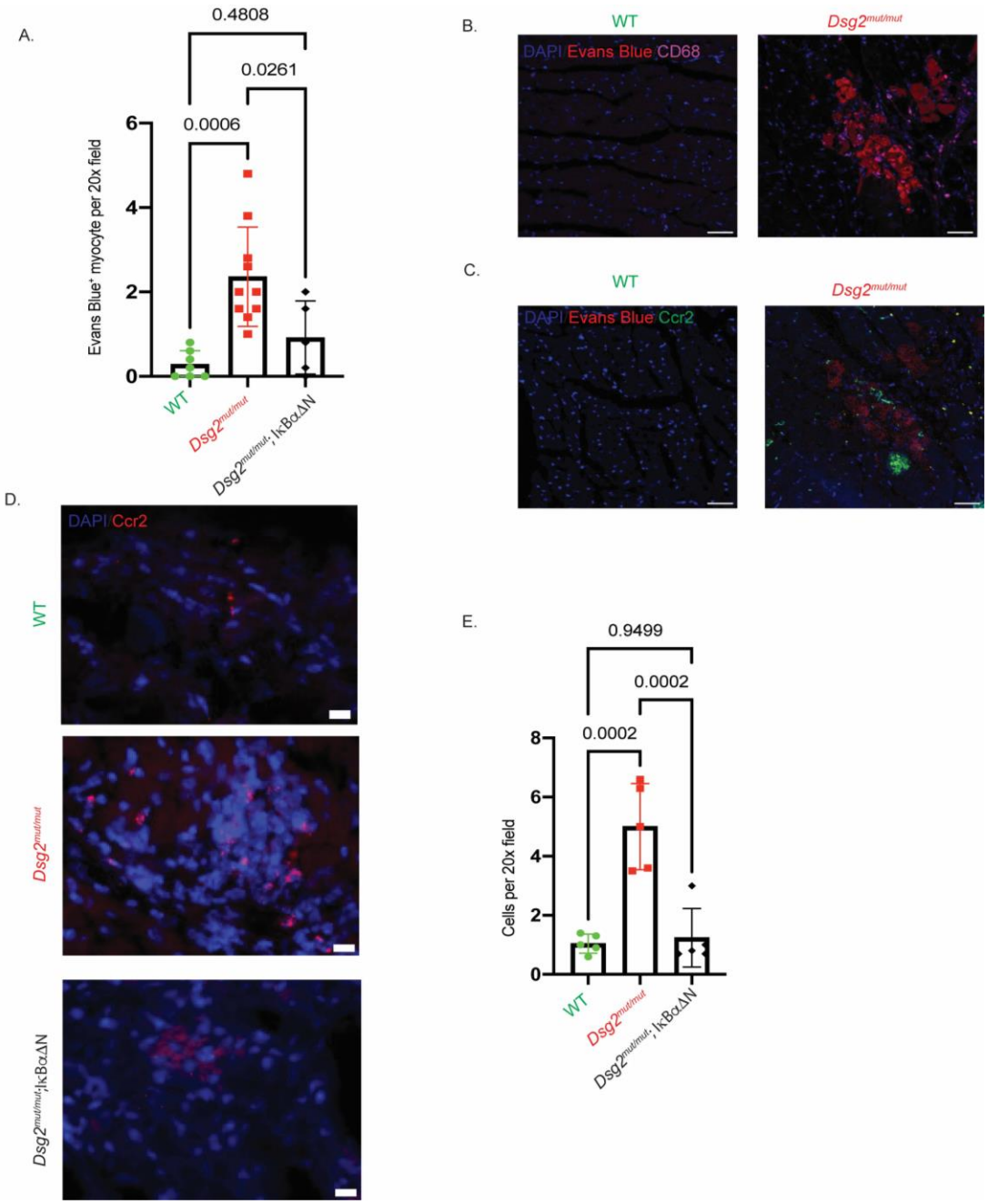

Figure 1. NFκB signaling in cardiac myocytes mobilizes CCR2^{+} macrophages to the heart. (A) Quantification of Evans Blue^{+} cardiac myocytes (per 20x) field in 16-week-old WT (n=7), *Dsg2$^{mut/mut}$* (n=10) and *Dsg2$^{mut/mut}$* X IκBαΔN (n=5) mice. (**B**) Representative immunostained myocardium showing CD68^{+} (violet) cells located in close proximity to Evans Blue^{+} cardiac myocytes (red). White scale bar, 40μm. (**C**) Representative RNA *in situ* hybridization images (RNAscope) showing CCR2^{+} (green) cells in close proximity to Evans Blue^{+} cardiac myocytes (red). White scale bar, 40μm. (**D**) Representative RNA *in situ* hybridization images (RNAscope) showing *Ccr2*$^{+}$ (red) cells in 16-week-old mice. White scale bar, 40μm. I Quantification of *Ccr2*$^{+}$ cells in mice. WT, n=10 samples; *Dsg2$^{mut/mut}$*, n=9 samples; *Dsg2$^{mut/mut}$* X IκBαΔN, n=10 samples. Data presented as mean±SEM; P-values inset; determined via one-way ANOVA with Tukey's posthoc analysis.

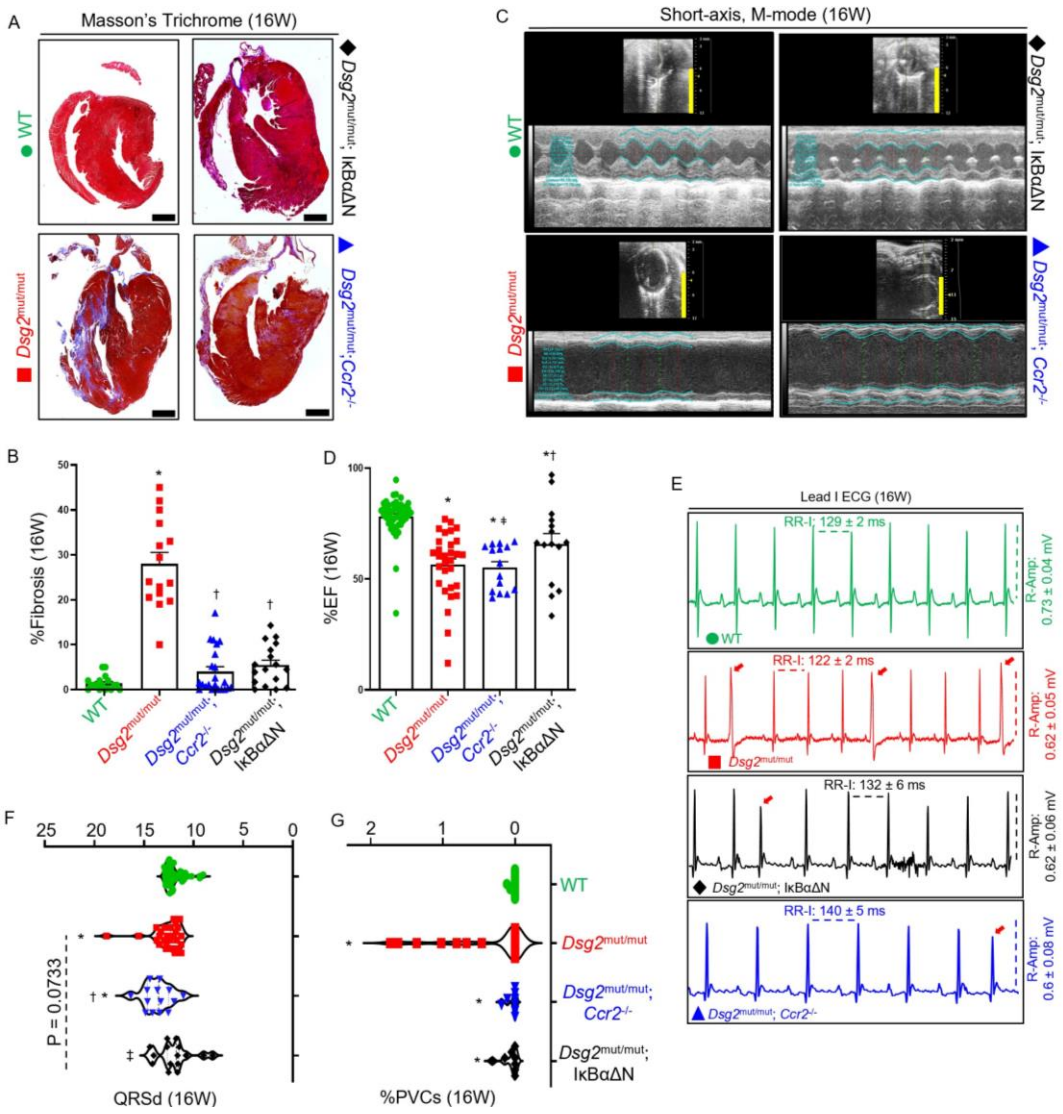

Figure 2. Blocking activation of NFκB signaling in cardiac myocytes mitigates myocardial injury and arrhythmias and preserves cardiac function in *Dsg2*$^{mut/mut}$ mice. (**A**) Representative trichrome-stained hearts from mice at 16 weeks of age (16W). Black scale bar, 1mm. (**B**) Percent (%) fibrosis at 16W; WT (n=18), *Dsg2*$^{mut/mut}$ (n=15), *Dsg2*$^{mut/mut}$ X IκBαΔN (n=17), and *Dsg2*$^{mut/mut}$ X *Ccr2*$^{-/-}$ mice (n=22). (**C**) Representative echocardiographs from 16W mice; yellow scale bar, 6mm. (**D**) Percent left ventricular ejection fraction (%LVEF). Note, preserved cardiac function in *Dsg2*$^{mut/mut}$ X IκBαΔN mice. WT (n=49), *Dsg2*$^{mut/mut}$ (n=30), *Dsg2*$^{mut/mut}$ X IκBαΔN (n=15), and *Dsg2*$^{mut/mut}$ X *Ccr2*$^{-/-}$ mice (n=15). *P<0.05 any cohort vs WT; †P<0.05 any cohort vs *Dsg2*$^{mut/mut}$; ‡P<0.05 *Dsg2*$^{mut/mut}$ X *Ccr2*$^{-/-}$ vs *Dsg2*$^{mut/mut}$ X IκBαΔN mice; using one-way ANOVA with Tukey's posthoc analysis. I Representative ECGs from 16W mice. Premature ventricular contractions (PVCs) are noted by red arrows. (**F, G**) QRS duration (QRSd) and percent PVCs (%PVCs), respectively, obtained from signal averaged ECGs. QRSd: WT (n=49), *Dsg2*$^{mut/mut}$ (n=27), *Dsg2*$^{mut/mut}$ X IκBαΔN (n=15), and *Dsg2*$^{mut/mut}$ X *Ccr2*$^{-/-}$ mice (n=14). %PVCs: WT (n=49), *Dsg2*$^{mut/mut}$ (n=30), *Dsg2*$^{mut/mut}$ X IκBαΔN (n=15), and *Dsg2*$^{mut/mut}$ X *Ccr2*$^{-/-}$ mice (n=15). Data presented as mean±SEM; *P<0.05 any cohort vs WT; †P<0.05 any cohort vs *Dsg2*$^{mut/mut}$; ‡P<0.05 *Dsg2*$^{mut/mut}$ X *Ccr2*$^{-/-}$ vs. *Dsg2*$^{mut/mut}$ X IκBαΔN mice; using one-way ANOVA with Tukey's posthoc analysis.

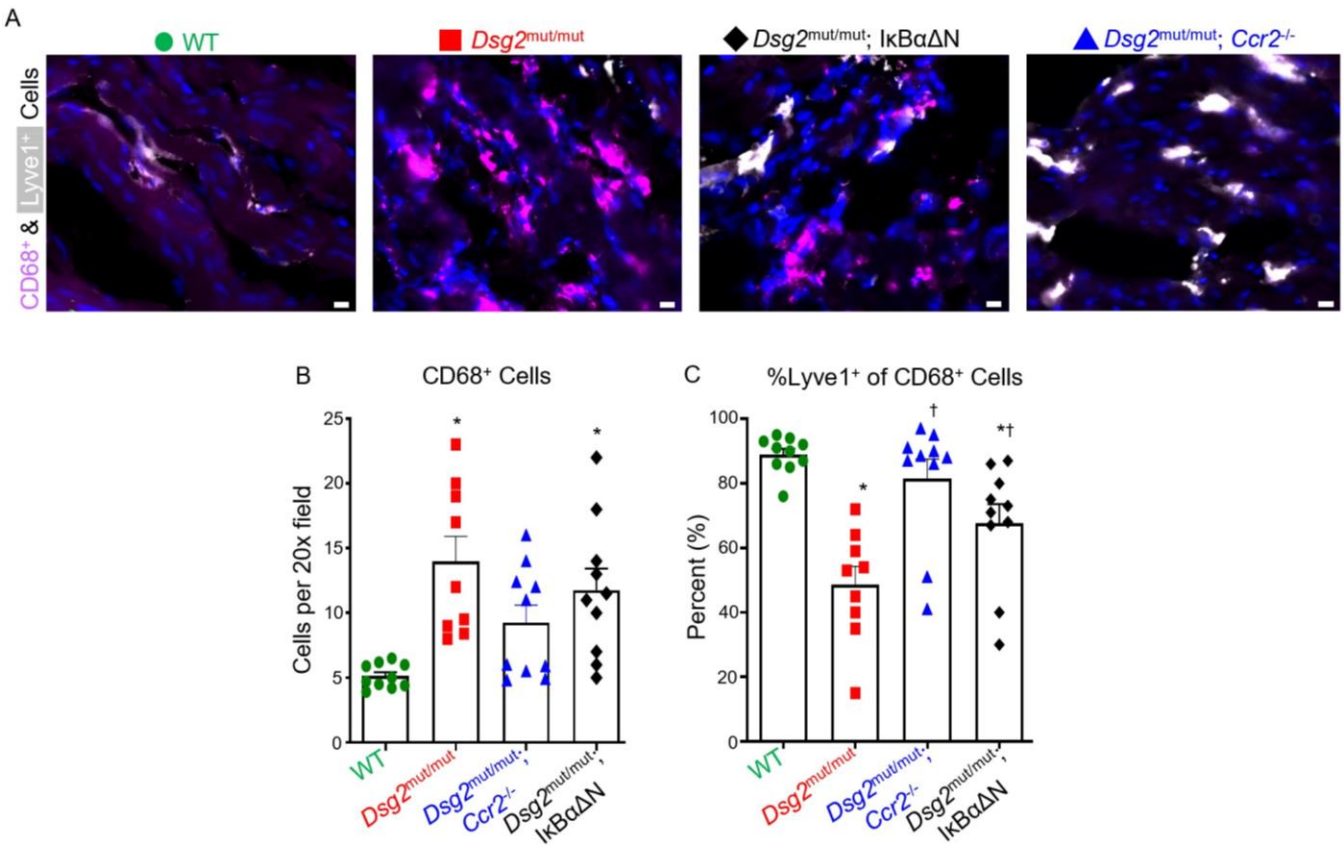

Figure 3. NFκB signaling in cardiac myocytes mobilizes inflammatory cells to the heart in *Dsg2*$^{mut/mut}$ mice. (**A**) Representative immunostained myocardial sections from 16-week-old (16W) mice showing CD68^{+} (violet) and Lyve1^{+} (white) cells. DAPI (blue); white scale bar, 40μm. (**B, C**) Quantification of CD68^{+} cells and Lyve1^{+} cells as a percentage of CD68^{+} cells in mice. Data presented as mean±SEM; n=10 for WT, *Dsg2*$^{mut/mut}$ X IκBαΔN and *Dsg2*$^{mut/mut}$ X *Ccr2*$^{-/-}$ mice and n=9 for *Dsg2*$^{mut/mut}$ mice. *P<0.05 any cohort vs WT; †P<0.05 any cohort vs *Dsg2*$^{mut/mut}$; using one-way ANOVA with Tukey's posthoc analysis.

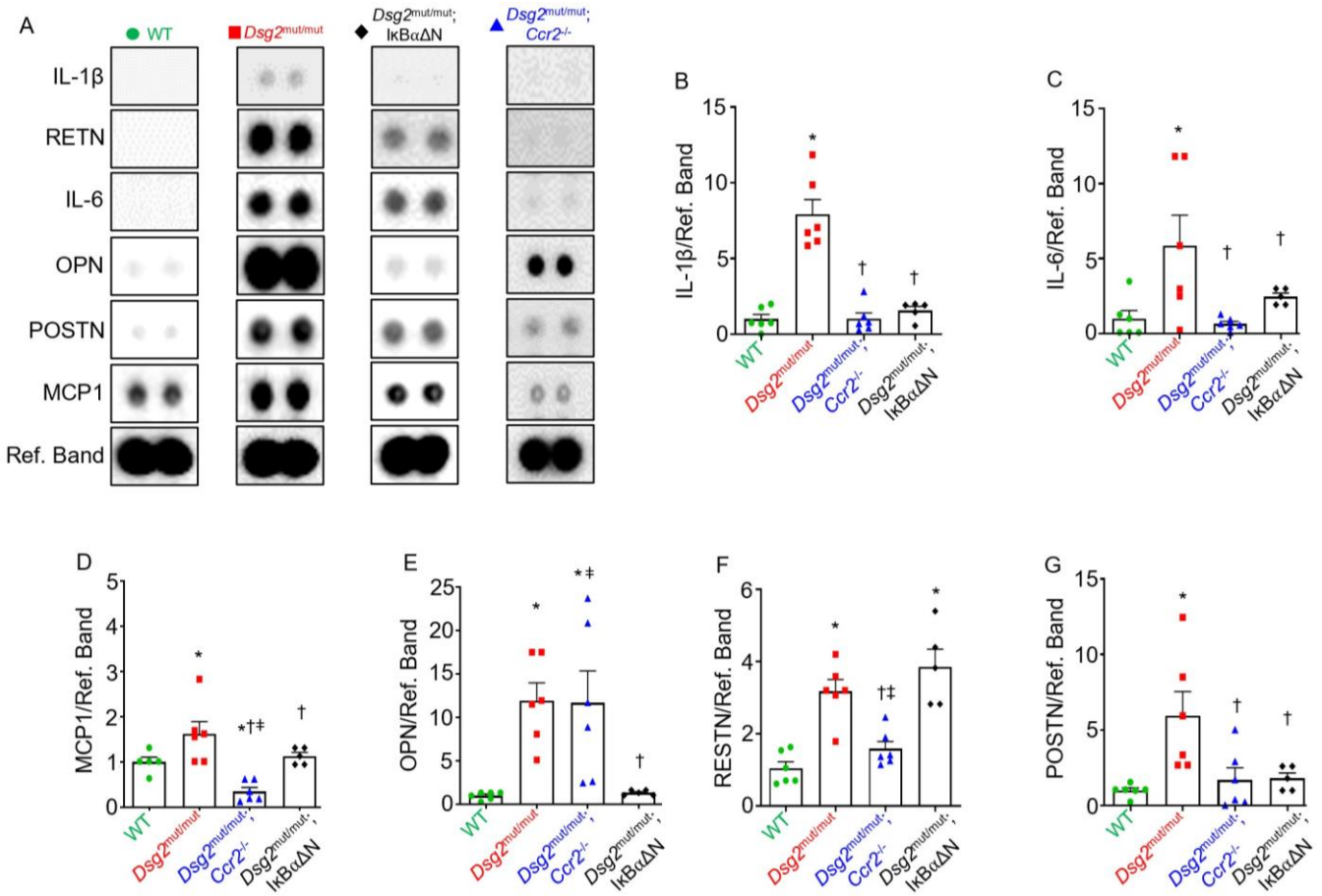

Figure 4. NFκB signaling in cardiac myocytes and actions of CCR2^{+} cells increase myocardial cytokines levels in *Dsg2$^{mut/mut}$* mice. (**A**) Representative immunoblots from myocardial cytokine arrays in WT (n=6), *Dsg2$^{mut/mut}$* (n=6), *Dsg2$^{mut/mut}$* X *Ccr2$^{-/-}$* (n=6) and *Dsg2$^{mut/mut}$* X IκBαΔN (n=5) mice. Ref. Band, Reference Band. (**B-G**) Bar graphs comparing levels of selected cytokines normalized to WT hearts. Data presented as mean±SEM; *P<0.05 any cohort vs WT; †P<0.05 any cohort vs *Dsg2$^{mut/mut}$*; ‡P<0.05 any cohort vs *Dsg2$^{mut/mut}$* X IκBαΔN using one-way ANOVA with Tukey's posthoc analysis.

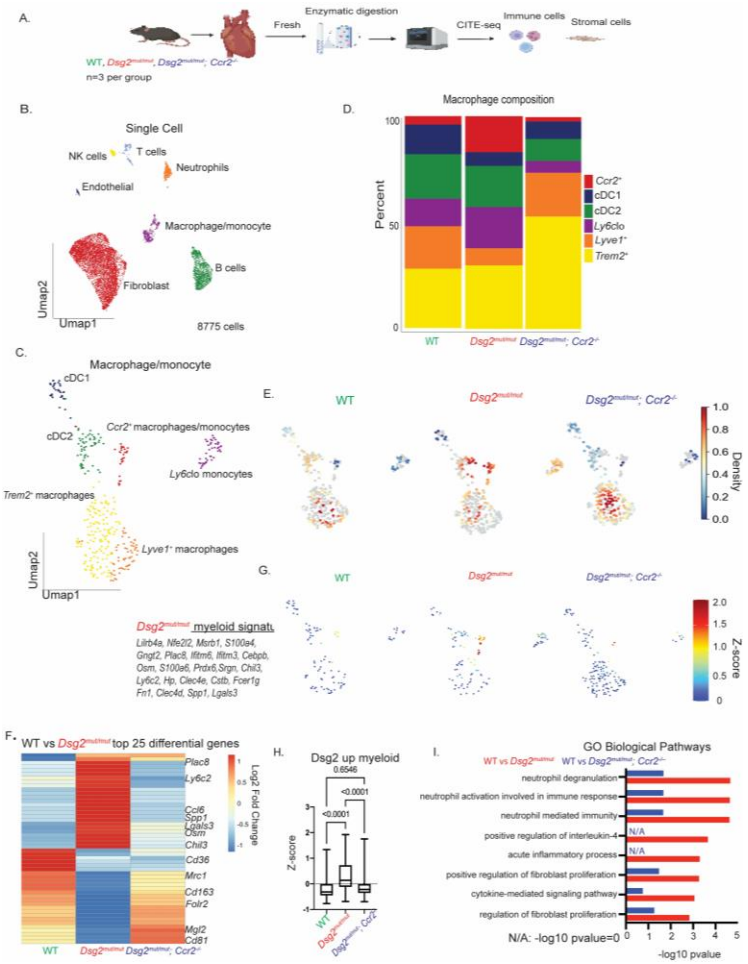

Figure 5. CITE-seq reveals expansion of CCR2^{+} inflammatory macrophages in hearts of *Dsg2$^{mut/mut}$* mice. (A) Schematic depicting design of CITE-seq experiments. Whole hearts from n=3 mice per condition were homogenized and enzymatically digested. **(B)** Uniform Manifold Approximation and Projection (UMAP) of 8,775 cells after quality control (QC) and data filtering using standard Seurat pipeline. **(C)** UMAP re-clustering of macrophage/monocyte population. **(D)** Composition graph showing proportion of different populations within the macrophage/monocyte cluster. **I** Gaussian kernel density estimation of cells within the macrophage/monocyte cluster across the indicated genotypes. **(F)** Heatmap of top 25 differentially expressed genes in the macrophage/monocyte cluster between WT and *Dsg2$^{mut/mut}$* mice with side-by-side comparison of the expression of those same genes from *Dsg2$^{mut/mut}$* X *Ccr2$^{-/-}$* mice. Example genes are annotated. (**G**) Z-score feature plot, overlaying an inflammatory gene signature derived from the heatmap in **F** (genes listed to the side) and displayed on the macrophage/monocyte UMAP projection split by genotype. (**H**) Graph of Z-score values for inflammatory gene signature derived from heatmap in **F** compared across genotypes. Data presented as a box-and-whisker plot. The five number summary (minimum, 25% IQR, median, 75% IQR, and maximum) as well as total number of values for each group is provided as follows; WT: -0.7688, -0.4471, -0.3135, -0.005451, 1.337, n=100, *Dsg2$^{mut/mut}$*: -0.6884, -0.1186, 0.1394, 0.7270, 1.923, n=124, *Dsg2$^{mut/mut}$* X *Ccr2$^{-/-}$:* -0.6941, -0.3559, -0.2186, -.005207, 1,752, n=145. P-values inset and determined via one-way ANOVA. (**I**) Top GO Biological pathways for the top 25 differentially upregulated genes in WT vs. *Dsg2$^{mut/mut}$* mice (red) and WT vs. *Dsg2$^{mut/mut}$* X *Ccr2$^{-/-}$* mice (blue) (derived from **F**).

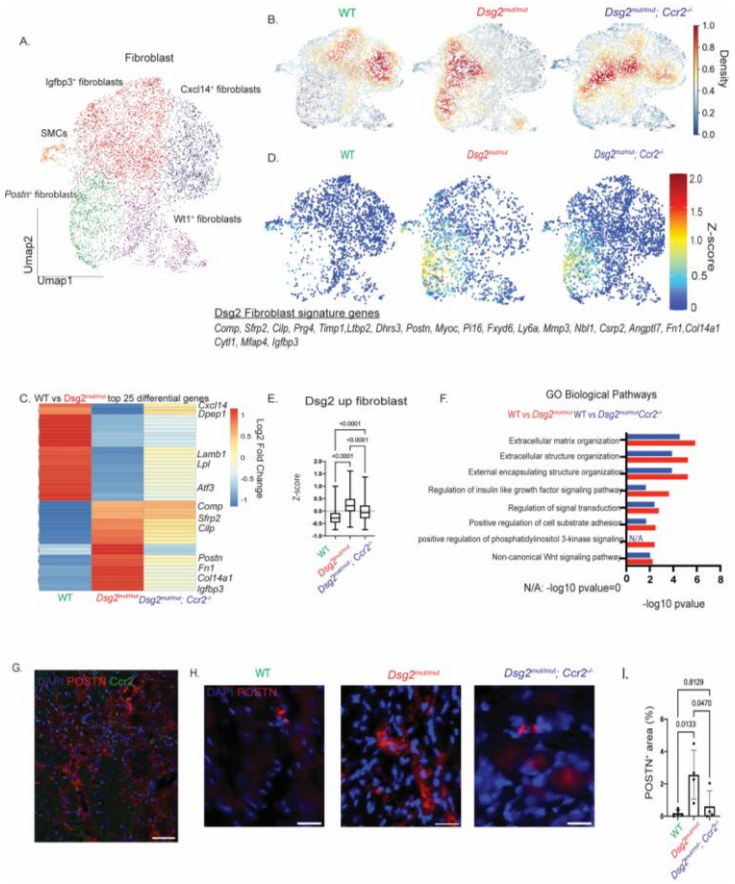

Figure 6. POSTN^{+} fibroblasts are expanded in *Dsg2$^{mut/mut}$* hearts through a CCR2^{+} monocyte- and macrophage-dependent mechanism. (**A**) UMAP re-clustering of fibroblast population. (**B**) Gaussian kernel density estimation of cells within the fibroblast cluster across the indicated genotypes. (**C**) Heatmap of top 25 differentially expressed genes in the fibroblast cluster between WT and *Dsg2$^{mut/mut}$* mice with side-by-side comparison of the expression of those same genes from *Dsg2$^{mut/mut}$* X *Ccr2$^{-/-}$* mice. Example genes are annotated. (**D**) Z-score feature plot, overlaying a fibroblast gene signature derived from the heatmap in **C** (genes listed to the side) and displayed on the fibroblast UMAP projection, split by genotype. I Graph of Z-score values for fibroblast gene signature derived from heatmap in **C** compared across genotypes. Data presented as a box-and-whisker plot. The five number summary (minimum, 25% IQR, median, 75% IQR, and maximum) as well as total number of values for each group is provided as follows; WT: -0.7450, -0.4597, -0.2805, -0.07749, 0.9996, n=1717, *Dsg2$^{mut/mut}$*: -0.6437, -0.008809, 0.2165, 0.4886, 1.611, n=1675, *Dsg2$^{mut/mut}$* X *Ccr2$^{-/-}$:* -0.7450, -0.2865, -0.06280, -.2262, 1,371, n=2625. P-values inset and determined by One-way ANOVA. (**F**) Top GO Biological pathways for the top 25 differentially upregulated genes in WT vs. *Dsg2$^{mut/mut}$* mice (red) and WT vs. *Dsg2$^{mut/mut}$* X *Ccr2$^{-/-}$* mice (blue) (derived from **C**). (**G**) Representative immunostained myocardium displaying colocalization of CCR2^{+} macrophages (green) with Periostin^{+} (POSTN^{+}) fibroblasts (red) at 16 weeks of age. White scale bar, 60μm. (**H**) Representative immunostained myocardium depicting POSTN^{+} (red) areas via immunofluorescence staining from mice aged 16 weeks from indicated genotypes. White scale bar, 40μm. (**I**) Quantification of POSTN^{+} area as a percentage of total area in mice of the indicated genotypes (P-values inset, determined via one-way ANOVA); WT (n=5); *Dsg2$^{mut/mut}$* (n=4); and *Dsg2$^{mut/mut}$* X *Ccr2$^{-/-}$*(n=4). Data presented as mean±SEM, n=4 per cohort, P-values inset and determined via one-way ANOVA.

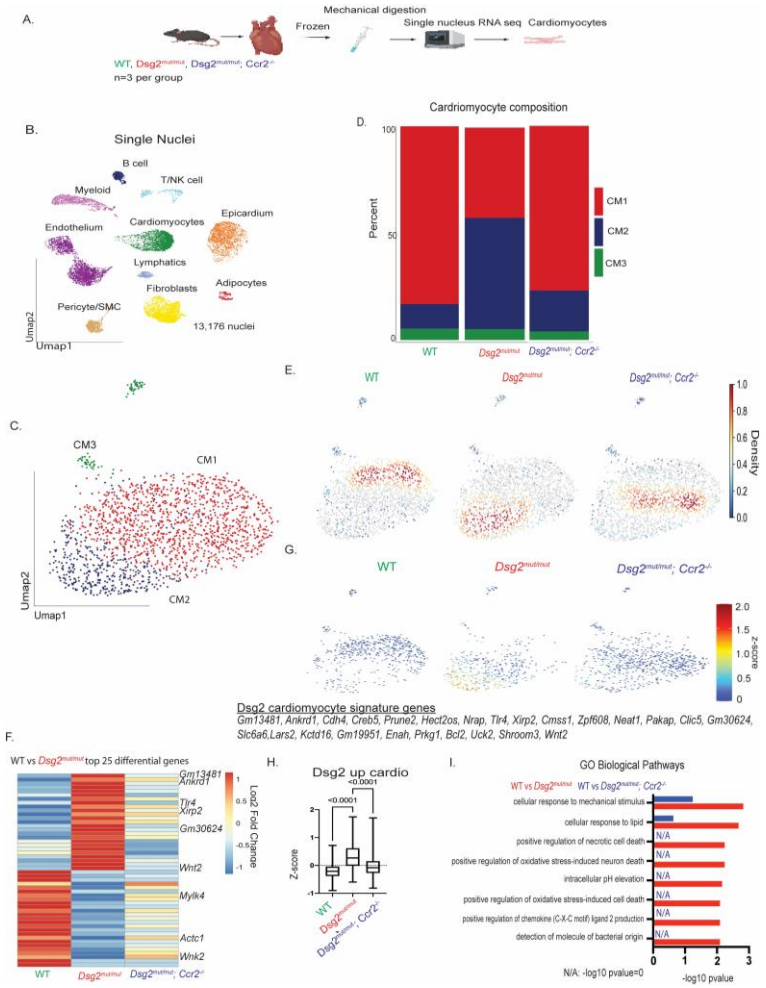

Figure 7. Single nucleus RNA sequencing (snRNA-seq) reveals a role for CCR2^{+} monocytes and macrophages in cardiac myocyte remodeling in ACM. (**A**) Schematic depicting design of snRNA-seq experiments. Frozen whole hearts (n=3 mice per group) were mechanically homogenized. (**B**) UMAP of 13,176 nuclei after QC and data filtering using standard Seurat pipeline. (**C**) UMAP re-clustering of cardiac myocyte population. (**D**) Composition graph showing proportion of different populations within the cardiac myocyte cluster. I Gaussian kernel density estimation of cells within the cardiac myocyte cluster across the indicated genotypes. (**F**) Heatmap of top 25 differentially expressed genes in the cardiac myocyte cluster between WT and *Dsg2$^{mut/mut}$* mice with side-by-side comparison of the expression of those same genes from *Dsg2$^{mut/mut}$* X *Ccr2$^{-/-}$*. Example genes are annotated. (**G**) Z-score feature plot, overlaying a cardiac myocyte gene signature derived from the heatmap in **F** (genes listed to the side) and displayed on the cardiac myocyte UMAP projection split by genotype. (**H**) Graph of Z-score values for cardiac myocyte gene signature derived from heatmap in **F** compared across genotypes. Data presented as a box-and-whisker plot. The five number summary (minimum, 25% IQR, median, 75% IQR, and maximum) as well as total number of values for each group is provided as follows; WT: -0.8992, -0.3708, -0.2077, -0.04161, 0.7185, n=564, *Dsg2$^{mut/mut}$*: -0.5954, -0.01474, 0.2699, 0.6183, 1.742, n=412, *Dsg2$^{mut/mut}$* X *Ccr2$^{-/-}$:* -0.8130, -0.2706, -0.08073, -.1536, 1,705, n=659. P-values inset and determined via one-way ANOVA. (**I**) Top GO Biological pathways for the top 25 differentially upregulated genes in WT vs. *Dsg2$^{mut/mut}$* mice (red) and WT vs. *Dsg2$^{mut/mut}$* X *Ccr2$^{-/-}$* mice (blue) (derived from **F**).

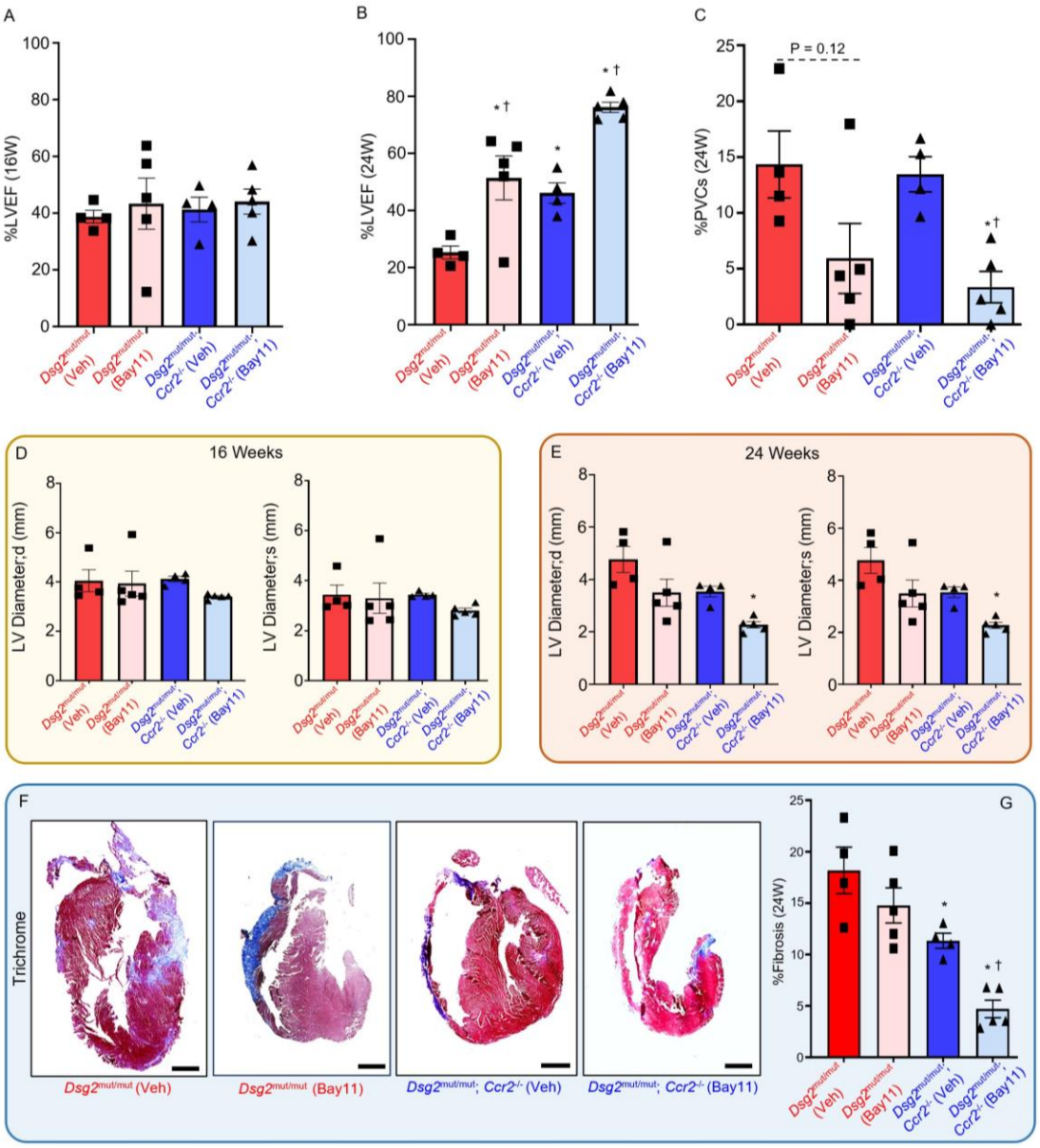

Figure 8. Contractile dysfunction is rescued in *Dsg2*$^{mut/mut}$ X *Ccr2*$^{-/-}$ mice via NFκB-inhibition. (**A, B**) Percent left ventricular ejection fraction (%LVEF) at 16 (16W) and 24 weeks (24) of age in *Dsg2*$^{mut/mut}$ and *Dsg2*$^{mut/mut}$ X *Ccr2*$^{-/-}$ mice treated for 8 weeks with either vehicle (Veh) or the NFκB inhibitor, Bay11-7082 (Bay11; 5mg/kg/day via continuous infusion at 0.11µL/hr for 8 weeks). Note, preserved cardiac function in Veh-treated *Dsg2*$^{mut/mut}$ X *Ccr2*$^{-/-}$ mice, whereas Bay11-treated *Dsg2*$^{mut/mut}$ X *Ccr2*$^{-/-}$ mice showed notable improvement in function following 8 weeks of Bay11 treatment. I Percent PVCs (%PVCs) at 24W. (**D, E**) Left ventricular internal diameter in diastole (LV Diameter;d) and systole (LV Diameter;s) at 16W and 24W in *Dsg2*$^{mut/mut}$ and *Dsg2*$^{mut/mut}$ X *Ccr2*$^{-/-}$ mice treated with either Veh or Bay11. (**F**) Representative trichrome-stained hearts (black scale bar, 1mm) and (**G**) percent (%) fibrosis at 24W from Veh-treated *Dsg2*$^{mut/mut}$ (n=4) and *Dsg2*$^{mut/mut}$ X *Ccr2*$^{-/-}$ mice (n=4), and Bay11-treated *Dsg2*$^{mut/mut}$ (n=5) and *Dsg2*$^{mut/mut}$ X *Ccr2*$^{-/-}$ mice (n=5) at 24W. Data presented as mean±SEM; *P<0.05 any cohort vs *Dsg2*$^{mut/mut}$ (Veh); †P<0.05 Bay11-treated mice vs Veh-treated mice within genotype; using one-way ANOVA with Tukey's posthoc analysis.

Table 1. Morphometric, echocardiographic, and electrocardiographic data at 16 weeks of age.

Parameter	WT	*Dsg2*$^{mut/mut}$	*Dsg2*$^{mut/mut}$ x *Ccr2*$^{-/-}$	*Dsg2*$^{mut/mut}$ X IκBαΔN
n-values	49	30	15	15
Morphometric				
LVM (mg)	82.9 ± 3.3	102.3 ± 4.8*	114.1 ± 9.7*‡	79.6 ± 3.5†
HW/BW (mg/g)	4.65 ± 0.1	5.32 ± 0.1*	4.99 ± 0.1*	4.85 ± 0.1†
RWT (mm)	0.63 ± 0.01	0.58 ± 0.03*	0.47 ± 0.02*†	0.47 ± 0.04*†
Echocardiographic				
FS (%)	50.3 ± 1.4	32.2 ± 1.9*	28.6 ± 1.7*	33.5 ± 2.8*
IVSd (mm)	0.97 ± 0.02	0.92 ± 0.03	0.84 ± 0.03*	0.82 ± 0.06*
IVSs (mm)	1.49 ± 0.02	1.29 ± 0.06*	1.19 ± 0.04*	0.90 ± 0.06*†‡
LVIDd (mm)	2.87 ± 0.06	3.38 ± 0.15*	3.76 ± 0.10*	3.60 ± 0.18*
LVIDs (mm)	1.46 ± 0.07	2.37 ± 0.18*	2.69 ± 0.11*	2.74 ± 0.21*
Electrocardiography				
Heart Rate (bpm)	473 ± 8	495 ± 7	440 ± 15*†	471 ± 17
RR-I (ms)	129 ± 2.1	122 ± 1.7	140 ± 4.7*†	132 ± 5.9†
PR-I (ms)	39.8 ± 0.7	40.5 ± 1.1	40.9 ± 2.5	41.9 ± 2.9*
Pd (ms)	10.9 ± 0.3	10.5 ± 0.5	12.1 ± 0.7*	11.7 ± 0.7*
QRSd (ms)	11.9 ± 0.1	12.7 ± 0.3*	13.6 ± 0.4*‡	11.9 ± 0.5†
P-Amp (mV)	0.06 ± 0.003	0.05 ± 0.01*	0.06 ± 0.01	0.05 ± 0.02*
R-Amp (mV)	0.73 ± 0.04	0.62 ± 0.1	0.60 ± 0.1	0.62 ± 0.1
Q-Amp (mV)	-0.05 ± 0.01	-0.09 ± 0.01*	-0.07 ± 0.01	-0.09 ± 0.02
S-Amp (mV)	-0.23 ± 0.01	-0.10 ± 0.03*	-0.14 ± 0.03	-0.05 ± 0.03*
PVCs (%)	0.03 ± 0.01	1.18 ± 0.6*	0.14 ± 0.1*	0.17 ± 0.1*

WT, wildtype; LVM, left ventricular mass; HW, heart weight; BW, body weight; RWT, relative wall thickness; FS, fractional shortening; IVSd/s, interventricular septum at end diastole or systole; LVIDd/s, left ventricular internal diameter at end diastole or systole; RR-I, R-R interval; PR-I, P-R interval; Pd, P-wave duration; QRSd, QRS-wave duration; P-Amp, P-wave amplitude; R-Amp, R-wave amplitude; Q-Amp, Q-wave amplitude; S-Amp, S-wave amplitude. PVCs, premature ventricular contractions; Data presented as mean±SEM, n-values inset. *P<0.05 any cohort vs WT; †P<0.05 any cohort vs. *Dsg2*$^{mut/mut}$ mice; ‡P<0.05 *Dsg2*$^{mut/mut}$ X *Ccr2*$^{-/-}$ vs. *Dsg2*$^{mut/mut}$ X IκBαΔN using one-way ANOVA with Tukey's post-hoc test.

Supplemental Figure 1. Flow cytometry gating scheme (A). Representative gating strategy for identifying lymphoid cell populations (B cells, $CD4^+$ T cells, and $CD8^+$ T cells) from the heart. **(B)** Representative gating strategy for identifying myeloid cell populations (neutrophils, monocytes, and macrophages) from the heart. Images are from 16-week-old WT mice and generated from FlowJo.

Supplemental Figure 2. Profiling of major immune cell populations over time in *Dsg2*$^{mut/mut}$ mice. Major immune populations (B cells, $CD4^+$ T cells, $CD8^+$ T cells, neutrophils, monocytes, macrophages) as a percentage of $CD45^+$ cells and $CCR2^-$ and $CCR2^+$ macrophages were profiled at several time points: 2 weeks, 4 weeks, 6 weeks, 10 weeks, and 16 weeks of age. N=3-6 mice per group per timepoint (specific numbers are included in Supplemental Data file). Data presented as mean±SEM; significance determined via 2-way ANOVA, and P-values inset.

Supplemental Figure 3. Disease characterization in adolescent *Dsg2*$^{mut/mut}$ and double mutant mice. (**A**) Representative trichrome immunostained hearts from 8-week-old mice (8W) WT (n=18), *Dsg2*$^{mut/mut}$ (n=17), *Dsg2*$^{mut/mut}$ X IκBαΔN (n=17), and *Dsg2*$^{mut/mut}$ X *Ccr2*$^{-/-}$ mice (n=18). Black scale bar, 1mm. (**B**) Percent (%) fibrosis at 8W and (**C**) percent left ventricular ejection fraction (%LVEF) from 8W WT (n=18), *Dsg2*$^{mut/mut}$ (n=27), *Dsg2*$^{mut/mut}$ X IκBαΔN (n=16), and *Dsg2*$^{mut/mut}$ X *Ccr2*$^{-/-}$ mice (n=15). Data presented as mean±SEM; *P<0.01 any cohort vs WT; using one-way ANOVA with Tukey's posthoc analysis.

Supplemental Figure 4. Double mutants have fewer induced-arrhythmias than *Dsg2*$^{mut/mut}$ mice. (**A**) Representative ECG tracings showing sinus rhythm, bigeminy, and ventricular tachycardia. **(B)**. Pie charts displaying portion of time each mouse spent in specified rhythm. Total ECG recording time was 20 minutes/mouse. N=5 mouse/cohort.

Supplemental Figure 5. Quality control and overview of CITE-seq data. (A) Violin plot of the RNA count per cell, split by genotype. **(B)** Violin plot of the number of genes per cell, split by genotype. **(C)** Violin plot of the percent of mitochondrial reads per cell split by genotype. **(D)** Violin plot displaying characteristic marker gene for each identified cell population. **I** Composition graph showing proportion of different populations within the entire CITE-seq data set. **(F)** Dot plot showing differentially expressed genes in each cell population between WT and *Dsg2*$^{mut/mut}$ mice. **(G)** Dot plot showing differentially expressed genes in each cell population between *Dsg2*$^{mut/mut}$ and *Dsg2*$^{mut/mut}$ X *Ccr2*$^{-/-}$. **(H)** Gaussian kernel density estimation of cells within the entire CITE-seq data set across the indicated genotypes.

Supplemental Figure 6. Characterization of macrophage/monocyte clusters. (A) Heat map of the top 10 genes by log 2-fold change enriched in each cluster. **(B)** Z-score feature plots for transcriptional signatures enriched in each sub cluster within the macrophage/monocyte population. Genes used for identification were selected based on enrichment from Seurat differential expression analysis.

Supplemental Figure 7. Characterization of fibroblast clusters. (A) Heat map of the top 10 genes by log 2-fold change enriched in each cluster. **(B)** Composition graph showing proportion of different populations within the fibroblast cluster. **(C)** Z-score feature plots for transcriptional signatures enriched in each sub-cluster within the fibroblast population. Genes used for identification were selected based on enrichment from Seurat differential expression analysis.

Supplemental Figure 8. Quality control and overview of snRNA-seq data. (A) Violin plot of the RNA count per cell, split by genotype. **(B)** Violin plot of the number of genes per cell, split by genotype. **(C)** Violin plot of the percent of mitochondrial reads per cell split by genotype. **(D)** Violin plot displaying characteristic marker gene for each identified cell population. **I** Composition graph showing proportion of different populations within the entire snRNA-seq data set. **(F)** Dot plot showing

differentially expressed genes in each cell population between WT and *Dsg2*$^{mut/mut}$ mice. **(G)** Dot plot showing differentially expressed genes in each cell population between *Dsg2*$^{mut/mut}$ and *Dsg2*$^{mut/mut}$ X *Ccr2*$^{-/-}$ mice. **(H)** Gaussian kernel density estimation of cells within the entire snRNA-seq data set across the indicated genotypes.

Supplemental Figure 9. Characterization of cardiac myocyte clusters. (A) Heat map of the top 10 genes by log 2-fold change enriched in each cluster. **(B)** Z-score feature plots for transcriptional signatures enriched in each sub cluster within the cardiac myocyte population. Genes used for identification were selected based on enrichment from Seurat differential expression analysis.

Supplemental Figure 10. Increased nuclear localization of active-NFκB in *Dsg2*$^{mut/mut}$ mice. (A, B) Representative immunostained mouse myocardium probed for DAPI (blue) and an antibody recognizing phosphorylated (Ser536) of NFκB (pNFκB Ser536) from 16-week-old WT, *Dsg2*$^{mut/mut}$, *Dsg2*$^{mut/mut}$ X IκBαΔN, and *Dsg2*$^{mut/mut}$ X *Ccr2*$^{-/-}$ mice. White arrowheads, perinuclear localization; yellow arrowheads, cytosolic localization; red arrowhead, nuclear localization in non-cardiomyocytes; white arrows, nuclear localization in cardiomyocytes. Large white scale bar, 50μm; small scale bar, 20μm. **I** Note, elevated pNFκB (Ser536) nuclear localization in *Dsg2*$^{mut/mut}$ mice, regardless of age. Large, black-filled circles, squares and triangles (or large open diamonds for *Dsg2*$^{mut/mut}$ X IκBαΔN mice) within bar graphs are the average of n=3 regions of interest (ROI) per mouse (n=20 mice/cohort). *P<0.05 for any cohort vs WT mice at 8 weeks of age (8W); $^{\alpha}$P<0.05 for any cohort vs WT mice at 16W; †P<0.05 for any cohort vs *Dsg2*$^{mut/mut}$ mice at 8W; ‡P<0.05 for any cohort vs *Dsg2*$^{mut/mut}$ mice at 16W; via one-Way ANOVA with Tukey's posthoc analysis. **(D)** Representative western immunoblot from cardiac lysates from 16W mice probed for GAPDH (red) and pNFκB (Ser536) (green) from WT, *Dsg2*$^{mut/mut}$, *Dsg2*$^{mut/mut}$ X IκBαΔN, and *Dsg2*$^{mut/mut}$ X *Ccr2*$^{-/-}$ mice (n=6/cohort). **I** Note, increased pNFκB (Ser536) levels in *Dsg2*$^{mut/mut}$

mice. Data presented as mean±SEM; *P<0.05 for any cohort vs WT mice, †P<0.05 for any cohort vs *Dsg2*$^{mut/mut}$ mice; via one-Way ANOVA with Tukey's posthoc analysis.

Supplemental Figure 11. Time course of disease in *Dsg2*$^{mut/mut}$ mice and NFκB inhibition study design. P1, postnatal day 1; W, week; ↓%EF, reduced percent ejection fraction; mouse clip art, Alzet minipump implantation at 16W and 20W of age.

Supplemental Table 1: Morphometric and electrocardiographic data at 8 weeks of age. WT, wildtype; LVM, left ventricular mass; HW, heart weight; BW, body weight; RWT, relative wall thickness; FS, fractional shortening; IVSd/s, interventricular septum at end diastole or systole; LVIDd/s, left ventricular internal diameter at end diastole or systole; RR-I, R-R interval; PR-I, P-R interval; Pd, P-wave duration; QRSd, QRS-wave duration; P-Amp, P-wave amplitude; R-Amp, R-wave amplitude; Q-Amp, Q-wave amplitude; S-Amp, S-wave amplitude. PVCs, premature ventricular contractions; Data presented as mean±SEM, n-values inset. *P<0.05 any cohort vs WT; †P<0.05 any cohort vs *Dsg2*$^{mut/mut}$ mice; ‡P<0.05 *Dsg2*$^{mut/mut}$ x *Ccr2*$^{-/-}$ vs *Dsg2*$^{mut/mut}$ x IκBαΔN using one-way ANOVA with Tukey's post-hoc test.

Supplemental Table 2. Fold-changes in cytokine levels in the hearts of *Dsg2*$^{mut/mut}$, *Dsg2*$^{mut/mut}$ X IκBαΔN, and *Dsg2*$^{mut/mut}$ X *Ccr2*$^{-/-}$ mice at 8 weeks of age. Data are presented as fold-change and P-values as compared to age-matched WT mice (n=5 mice/cohort). P-values were determined using one-way ANOVA with Tukey's posthoc test.

Supplemental Table 3: Fold-changes in cytokine levels in the hearts of *Dsg2*$^{mut/mut}$, *Dsg2*$^{mut/mut}$ X IκBαΔN, and *Dsg2*$^{mut/mut}$ X *Ccr2*$^{-/-}$ mice at 16 weeks of age. Data are presented as fold-change and P-values as compared to age-matched WT mice (n=5 mice/cohort). P-values were determined using one-way ANOVA with Tukey's posthoc test.

Supplemental Table 4. Morphometric and electrocardiographic data at 24 weeks of age in *Dsg2*$^{mut/mut}$ and *Dsg2*$^{mut/mut}$ X *Ccr2*$^{-/-}$ mice with Bay11-7082 or vehicle. LVM, left ventricular mass; HW, heart weight; BW, body weight; RWT, relative wall thickness; FS, fractional shortening; IVSd/s, interventricular septum at end diastole or systole; LVIDd/s, left ventricular internal diameter at end diastole or systole; RR-I, R-R interval; PR-I, P-R interval; Pd, P-wave duration; QRSd, QRS-wave duration; P-Amp, P-wave amplitude; R-Amp, R-wave amplitude; Q-Amp, Q-wave amplitude; S-Amp, S-wave amplitude. PVCs, premature ventricular contractions; Data presented as mean±SEM, n-values inset. *P<0.05 any cohort vs *Dsg2*$^{mut/mut}$ mice (Vehicle); †P<0.05 *Dsg2*$^{mut/mut}$ x *Ccr2*$^{-/-}$ (Bay11-7082) vs *Dsg2*$^{mut/mut}$ x *Ccr2*$^{-/-}$ (Vehicle) using one-way ANOVA with Tukey's post-hoc test.

SUPPLEMENTAL METHODS

Echocardiography was performed using a 2100 Vevo Visualsonic machine equipped with a 40 MHz ultrahigh frequency linear array microscan transducer. Images were obtained according to the American Society of Echocardiography guidelines for animals (44). Short-axis, m-mode and parasternal long-axis images, B-mode images at the level of the papillary muscles were acquired at a sweep speed of 200 mm/s, as previously described (6-8). Measurements obtained from three to five echocardiographic images for each mouse were averaged to assess left ventricular ejection fraction (EF) and wall and chamber dimensions (6-8).

Body surface ECGs were performed in lightly anesthetized mice (nose cone delivery of 1.5 – 2% isoflurane vaporized in 100% O_2) using PowerLab to obtain Lead I ECG recordings, as previously described (6-8). Recordings were analyzed using the ECG Analysis Add-on Software from LabChart Pro (LabChart Pro 8, MLS360/8, AD Instruments). Signal-averaged ECGs (SAECGs) constructed from 10-minute recordings using LabChart were used to measure ECG durations, intervals, and wave and

amplitude parameters. The entire 10-minute ECG recording for each animal was analyzed to determine the percentage of PVCs by total beats. Once 16-week ECG studies were completed, mice were euthanized and hearts excised for histologic, immunohistochemical, cytokine and sequencing analyses.

Arrhythmia induction studies were performed in lightly anesthetized mice (nose cone anesthesia, via delivery of 2% isoflurane vaporized in 100% O_2) using the Roden Surgery Monitor Plus system (Indus Technologies) to obtain recordings. Baseline ECGs were measured for 30 seconds before intraperitoneal infusion of caffeine (120mg/kg) and dobutamine (60μg/kg)(45) and further recorded for 20 minutes. Recordings were analyzed using LabChart Reader and ECG sinus rhythms vs arrhythmias were identified and analyzed as Pie Charts displayed as portions of time spent in specified rhythm.

Myocardial fibrosis was measured in long-axis sections of formalin-fixed, paraffin-embedded hearts cut at 5μm and stained with Masson's trichrome stain. The total amount of right and left ventricular section area occupied by fibrosis was determined by the sum of all fibrotic areas divided by total myocardial area using ImageJ version 1.53e software (8).

Flow cytometry was performed in WT and *Dsg2*$^{mut/mut}$ mice at 2 weeks, 4 weeks, 6 weeks, 10 weeks, and 16 weeks of age. Hearts were minced on ice with a razor blade, transferred to a 15mL conical tube containing 3mL DMEM with 170μL collagenase IV (250U/mL final concentration), 35μL DNAse1 (60U/mL), and 75μL hyaluronidase (60U/mL), and incubated at 37°C for 45 min with agitation. Thereafter, the digestion reaction was quenched with 5mL of HBB buffer (2% FBS and 0.2% bovine serum albumin (BSA) in HBSS), passed through 40μm filters into a 50mL conical tube and transferred back into a 15mL conical tube to obtain tighter pellets. Samples were then spun down at 4°C, 1200 rpm for 5 min and the supernatant was discarded. Pellets were resuspended in 1mL ACK Lysis buffer (Gibco, Cat. No. A10492-01) and incubated at room temperature for 5 min, followed by the addition of 9mL DMEM and centrifugation (4°C, 5 min, 1200 rpm). Supernatant was discarded and the

pellets were resuspended in 2mL FACS buffer (2% FBS and 2mM EDTA in calcium/magnesium free PBS); centrifugation was repeated in above conditions and supernatant aspirated. Samples were stained with antibodies for 30 min at 4 degrees in the dark. Solution was washed 3x with FACS buffer following same centrifugation as above and then resuspended in 300µL of FACS buffer. Samples were run on a Cytek Aurora (Cytek Biosciences). Subsequent analysis was performed on FlowJo. Complete list of antibodies used are available in supplemental data.

Immunohistochemistry, Evans Blue staining, and western immunoblots were performed to measure the number of CD68 and Lyve1-expressing (24, 46) cells in hearts of WT, *Dsg2*$^{mut/mut}$ and double mutant mice at 16 weeks of age. Isolated hearts were perfused with 1X PBS and fixed overnight in 4% paraformaldehyde in 1X PBS at 4°C. After being dehydrated in 30% sucrose in 1X PBS at 4°C overnight, they were embedded in O.C.T. (Sakura, Cat. No. 4583) and stored at -80ºC for 10 min. They were then sectioned at 12 µm using a Leica cryostat, mounted on positively charged slides, and stored at -20ºC. For staining, the following steps were performed at room temperature and protected from light. Slides were brought to room temperature for 5 min and washed in 1X PBS for 5 min. Sections were permeabilized in 0.25% Triton-X in 1X PBS for 5 min and blocked in 5% BSA in 1X PBS for 1 hr. Sections were then stained with primary antibodies (rat anti-CD68, BioLegend Cat. No. 137002, at 1:400; rabbit anti-Lyve1, Abcam Cat. No. 14917, at 1:200; rabbit anti-Periostin, Abcam Cat. No. 215199, at 1:200; or rabbit anti-pNFκB Serine 536, GeneTex Cat. No. GTX55114, at 1:500) diluted in 1% BSA in 1X PBS for 1 hr. Sections were then washed 3 times for 5 min each with 1X PBS-Tween. After washing, appropriate secondary antibodies (goat anti-rat Alexa Fluor 555, Invitrogen Cat. No. A21434; donkey anti-rabbit Alexa Fluor 647, Abcam Cat. No. ab150075; or goat anti-rabbit Alexa Fluor 555, Invitrogen Cat. No. A21428; all at 1:1000) were added for 1 hr at 1:1000 in 1% BSA in 1X PBS. Slides were again washed 3 times for 5 min each with 1X PBST, and then mounted with DAPI

mounting media (Millipore Sigma, Cat. No. F6057) and cover slipped. Slides were stored at 4ºC, protected from light, and imaged within 1 week using the 20x objective lens of a Zeiss LSM 700 confocal microscope. For quantification, ten 20x fields were prepared from each mouse heart. Cell numbers and area percentages were quantified in Zen Blue, and data were displayed as the average per 20x field per mouse. 16-week-old WT, *Dsg2*$^{mut/mut}$, and *Dsg2*$^{mut/mut}$ X IκBαΔN were injected intraperitoneally with 2mg/kg of Evans Blue (Sigma Aldrich CAS no. 314-13-6) 48 hours and 24 hours prior to harvesting. Hearts were isolated, fixed, and sectioned as above. Slides were visualized as above and quantification for Evans Blue positive myocytes was performed as above.

For western immunoblots, myocardium was lysed in RIPA Buffer (ThermoFisher, Cat. No. 89900) containing 1:100 protease and phosphatase inhibitor cocktails (Sigma-Aldrich) and protein was quantified via the Pierce BCA protein assay kit (Life Technologies). Forty micrograms of myocardial lysates were run and separated on 4-12% BisTris gels (NuPage, Invitrogen) with 1X MOPS Running Buffer (Invitrogen). Gels were transferred to nitrocellulose membranes then blocked for 1hr in 1X PBS containing 5% BSA and 0.1% Tween-20 at room temperature. Immunoblots were then probed with rabbit anti-pNFκB Serine 536 (GeneTex Cat. No. GTX55114, at 1:1000) and mouse anti-GAPDH (ThermoFisher Cat. No. Cat MA1-16757 at 1:2000) at 4°C overnight. The following day, immunoblots were washed three times with 1X PBST then probed with species-specific IRDye secondary antibodies (LiCor IRDye 800CW or IRDye 680RD at 1:10,000) for 1hr at room temperature, washed three times with 1X PBST, and imaged via the LI-COR Odyssey imaging system.

RNA-scope *in situ* hybridization was performed as previously (24), which was used to identify and quantify CCR2^{+} cells in hearts of WT, *Dsg2*$^{mut/mut}$ and double mutant mice at 16 weeks of age. Hearts were fixed and dehydrated, and sections were cut as above. CCR2 (Cat. No. 433271) RNA-Scope probes produced by ACDBio were used. RNA was visualized using RNA-Scope Multiplex

Fluorescent Reagent kit v2 Assay (ACDBio 323100). Fluorescent images were collected using a Zeiss LSM 700 laser scanning confocal microscope and quantification was performed as above.

Myocardial cytokines were measured using Proteome Profiler Mouse XL Cytokine Array Kits (R&D Systems, Cat. No. ARY028) (6). Frozen heart samples were lysed in RIPA buffer containing 1:100 protease and phosphatase inhibitor cocktails. Protein content in lysates were quantified via BCA assay and 40µg/µl of protein lysate were probed on cytokine array blots. Following the manufacturer's protocol, blots were incubated with ECL substrate, imaged on an Azure Biosystems 400 imager and analyzed using Quick Spots image analysis software (Version 25.5.1.2, Ideal Eyes Systems).

Sample preparation for CITE-seq was performed as previously (24, 29). Freshly isolated hearts from 16-week-old WT, *Dsg2*$^{mut/mut}$ and *Dsg2*$^{mut/mut}$ X *Ccr2*$^{-/-}$ mice (n=3 per group) were prepared as described previously for flow cytometry and then the TotalSeq A 277 panel (BioLegend, Cat. No. 199901) antibody cocktail was resuspended in 100µL of FACS buffer and added to each sample. The combined 100µL were used to resuspend the pellet with the addition of 1µL of DRAQ5 (5mM solution Thermo Fisher Scientific, Cat. No. 564907) and incubated on ice for 30 min. Solution was washed 3x with FACS buffer following same centrifugation as above and then resuspended in 300µL of FACS buffer and 1uL DAPI (BD Biosciences, Cat. No. 564907) and filtered into filter top FACS tubes. First singlets were gated and subsequent DRAQ5+/DAPI- events were collected in 300µL cell resuspension buffer (0.04% BSA in PBS) – collected cells were centrifuged as above and resuspended in collection buffer to a target concentration of 1,000 cells/µL. Cells were counted on a hemocytometer before proceeding with the 10x protocol.

Sample preparation for single nuclei RNA-seq (snRNA-seq): was performed as previously described (24). Frozen hearts from 16-week-old WT, *Dsg2*$^{mut/mut}$ and *Dsg2*$^{mut/mut}$ X *Ccr2*$^{-/-}$ mice (n=3 per group) were minced with a razor blade and transferred into a 5mL Dounce homogenizer containing 1–

2mL chilled lysis buffer (10 mM Tris-HCl, pH 7.4, 10 mM NaCl, 3 mM $MgCl_2$ and 0.1% NP-40 in nuclease-free water). Samples were gently homogenized using five passes without rotation, and then incubated on ice for 15 min. Lysate was gently passed through a 40µm filter into 50mL conical tube, followed by rinsing the filter once with 1ml lysis buffer and transfer of lysate to a new 15mL conical tube. Nuclei were then centrifuged at 500*g* for 5 min at 4°C, followed by resuspension in 1mL nuclei wash buffer (2% BSA and 0.2 U /µL Rnase inhibitor in 1X PBS) and filtered through a 20µm pluristrainer into a fresh 15mL conical tube. Centrifugation was repeated according to the above parameters. Supernatant was then removed, and nuclei were resuspended in 300µL nuclei wash buffer and transferred to a 5mL tube for flow sorting. Then, 1µl DRAQ5 (5 mM solution; ThermoFisher, Cat. No. 62251) was added, mixed gently and allowed to incubate for 5 min before sorting. $DRAQ5^+$ nuclei were sorted into nuclei wash buffer. Recovered nuclei were centrifuged again under the above parameters and were gently resuspended in nuclei wash buffer to a target concentration of 1,000 nuclei/µL. Nuclei were counted on a hemocytometer.

CITE-seq library preparation: was performed as previously described (24, 29). Collected cells were processed using the single Cell 3' Kit v 3.1 (10x Genomics PN: 1000268). 10,000 cells were loaded onto ChipG (PN: 1000121) for GEM generation. Reverse transcription, barcoding and complementary DNA amplification of the RNA and ADT tags were performed as recommended in the 3' v3.1 chromium protocol. Single-cell libraries were prepared using the single Cell 3' Kit v 3.1 following a modified 3' v3.1 assay protocol (User Guide CG000206) to concurrently prepare gene expression and TotalSeq A antibody derived tag (ADT) libraries as recommended by BioLegend. 1µl of 0.2uM ADT Additive Primer (CCTTGGCACCCGAGAATT*C*C) and 15µl of cDNA Primers (PN: 2000089) were used to amplify cDNA. ADT libraries were amplified with a final concentration of 0.25 µM SI Primer (AATGATACGGCGACCACCGAGATCTACACTCTTTCCCTACACGACGC*T*C)

and 0.25 µM TrueSeq Small RNA RPI primer (CAAGCAGAAGACGGCATACGAGAT [6nt index] GTGACTGGAGTTCCTTGGCACCCGAGAATTC*C*A) using 11 cycles. Gene expression libraries were indexed using Single Index Kit T Set A (PN: 2000240). Libraries were sequenced on a NovaSeq 6000 S4 flow cell (Illumina).

snRNA-seq library preparation: Nuclei were processed using the Chromium Single Cell 5′ Reagent V2 kit from 10X Genomics (PN-1000263), as previously described (24). A total of 10,000 nuclei per sample were loaded into a Chip K for GEM generation. Reverse transcription, barcoding, complementary DNA amplification and purification for library preparation were performed according to the Chromium 5′ V2 protocol. Sequencing was performed on a NovaSeq 6000 platform (Illumina).

CITE-seq alignment, quality control and cell type annotation: Raw fastq files were aligned to the mouse GRCh38 reference genome (v) using CellRanger (10x Genomics, v6.1) with the antibody capture tag for the TotalSeqA 277 antibodies, as previously described (24, 29). Subsequent quality control, normalization, dimensional reduction, and clustering were performed in Seurat v4.0. Following normalization, quality control was performed and cells passing the following criteria were kept for downstream processing: 200 < nFeature_RNA < 6000 and 1,000 < nCount_RNA < 30,000 and percentage mitochondrial reads < 10%. Raw RNA counts were normalized and scaled using SCTransform regressing out percent mitochondrial reads and nCount RNA. Principal component (PC) analysis was performed on normalized RNA counts and the number of PCs used for further processing was determined by fulfilling the following criteria: PCs exhibited cumulative percent >90% and the percent variation associated with the PCs was < 5%. Weighted nearest neighbor clustering (WNN) was performed with the significant RNA PCs and normalized proteins directly without PCA as previously outlined with the FindMultiModalNeighbors function in Seurat. Subsequently, a uniform manifold approximation (UMAP) embedding was constructed and FindClusters was used to unbiasedly cluster

cells. Clustering was performed for a range of different resolutions (0.1-0.8 at 0.1 intervals) and differential gene expression using the FindAllMarkers function and a Wilcoxon Rank Sum test with a logFC cutoff of 0.25 and a min.pct cut-off of 0.1. Clusters were annotated using canonical gene and protein markers and subsequent violin plots were created to assess clean separation of clusters into distinct cell types. To cluster cell types into distinct cell states, the cell type of interest was subsetted, re-normalized, computed PCAs, computed UMAPs, and clustered data at a range of resolutions. DE analysis was then used to identify marker genes for each cell state and constructed a dot-plot or heatmap to assess clustering separation. Using the top marker genes, gene set z-scores were calculated and plotted in UMAP space.

snRNA-seq alignment, quality control and cell type annotation were performed as previously described (24, 29). Raw fastq files were aligned to the mouse GRCh38 reference genome (v) using CellRanger (10x Genomics, v6.1). Subsequent quality control, normalization, dimensional reduction, and clustering were performed in Seurat v4.0. Following normalization, quality control was performed and cells passing the following criteria were kept for downstream processing: 500 < nFeature_RNA < 4000 and 1,000 < nCount_RNA < 16,000 and percentage mitochondrial reads < 3%. To remove doublets, Scrublet was run with a cutoff score of >0.25 to identify doublets. Following doublet removal, raw RNA counts were normalized and scaled using SCTransform. PCs were then calculated, and an elbow plot was generated to select the cutoff for significant PCs to use for downstream analysis. UMAP dimensional reduction was then computed using the selected significant PCs. Unsupervised clustering was then performed using the FindNeighbors and FindClusters function, again using the selected significant PC level as above, calculating clustering at a range of resolutions between 0.1–0.8 at intervals of 0.1. Differential gene expression was performed using the FindAllMarkers command and a Wilcoxon Rank Sum test with a logFC cutoff of 0.25 and a min.pct cut-off of 0.1. Clusters were

annotated in the same manner as the CITE-seq analysis. Subsequent sub-clustering and DE analysis was performed in the same manner as above.

Density shift calculations: R was used to compute cell type composition across genotypes. To assess shifts in cell density within both the global object and individual cell types, the .rds object was converted to a .h5ad file format and scanpy.tl.embedding function which employs a Gaussian kernel density estimation of cell number was used within the UMAP embedding, as previously described (24, 29). Density values were scaled from 0-1 within that category.

Pathway analysis: Statistically significant DE genes were used to perform pathway analysis via EnrichR (https://maayanlab.cloud/Enrichr/). Pathway enrichment values were downloaded as .csv files and plots generated in Prism.

Author contributions:

Stephen P. Chelko (**SPC**), Vinay Penna (**VRP**), Morgan Engel (**ME**), Emily Shiel (**EAS**), Ann M. Centner (**AMC**), Waleed Farra (**WF**), Elisa N. Cannon (**ENC**), Maicon Landim-Vieira (**MLV**), Niccole Schaible (**NS**), Kory Lavine (**KL**) Jeffrey E. Saffitz (**JES**).

SPC, JES, and KL conceived and designed the study. SPC,[α] VRP,[α] ME, EAS, AMC, WF, MLV, and NS performed experiments. ENC and WF were responsible for maintaining, crossing, and genotyping mice. SPC, JES, VP and KL drafted and revised the manuscript. SPC, VRP, ME, MLV, and NS were responsible for data acquisition and analysis. JES and KL provided expert input, training, and data interpretation. **[α]Co-first authors:** SPC and VRP performed equal contributions to this body of work – in both technical and conceptual design.